**The PDF file includes:**

Supplementary Text

Supplementary Figures 1 to 22

Supplementary Tables 1 to 5

References

Corresponding author: etienne.legrain@ulb.be

# Supplementary Text

## Orbital- to millennial-scale variability of the new $CO_2$ record

Our multi-centennial-scale $CO_2$ record represents a substantial improvement in temporal resolution compared to the existing millennial-scale $CO_2$ record measured on the Vostok ice core over the 260-190 ka time interval [1] (Supplementary Figure 1).

At orbital-scale, our new dataset confirms that the Termination III (TIII) (~248-242 ka) is much more pronounced than the so-called TIIIa [2] (~223-217 ka), with a global $CO_2$ rise of 79 and 48 ppm, respectively. This pattern is similar to the one observed in the Antarctic surface temperature reconstruction from the EDC ice core [3]. Between 241 and 227 ka, the progressively-decreasing plateau of $CO_2$ concentrations appears decoupled from East Antarctic surface temperature (Fig. 2). Such decoupling was already described during MIS 5 [4,5] and more globally during the low obliquity period of the past 800 ka [6]. This pattern, possibly linked to the dynamics of the Southern Ocean under low-obliquity phase [7], is confirmed by our new $CO_2$ record and it occurs during a period characterised by the lowest obliquity values of the past 800 ka (Fig. 2).

At millennial-scale, we identify a high-variability period between 251.4 and 248.9 ka at the onset of TIII. This millennial-scale variability was not observed in the previous Vostok $CO_2$ record, probably due to the lack of resolution over this period [1]. However, this event was already described in the Antarctic site temperature [2] and Asian speleothem $\delta^{18}O$ records [8]. Such two-phase deglaciation visible in the $CO_2$ record was also observed during TI.

## Definition of CDJs and associated thresholds

CDJs have been defined by ref. [9] as an increase of atmospheric $CO_2$ concentrations higher than 5 ppm and at a growth rate higher than 1.5 ppm/century. Both of these thresholds are applied to a processed $CO_2$ record where only sub-millennial-scale variability has been preserved. This definition has two main consequences when discussing the occurrence of CDJ: (i) CDJs correspond to the largest and most abrupt events in centennial scale variability and do not include all the increases of $CO_2$ concentrations at centennial-scale. The two thresholds act as low-band filters that only select the most prominent $CO_2$ increase events. Accordingly, the influence of the obliquity is only investigated for the largest centennial-scale $CO_2$ concentration changes, and not all the $CO_2$ centennial-scale variations. This also eases comparison with model results as these events are clearly above the centennial background variability. (ii) CDJs are objectively and systematically determined by a statistical method, and the consequent classification of a variation as CDJ is binary: if it matches the two criteria, the event is considered as a CDJ. If one of the two criteria is not reached, the event is not classified as a CDJ.

To ensure consistency with the original study [9] that defined the CDJ events, we also used the threshold values of 1.5 ppm/century for the growth rate and 5 ppm for the amplitude of the CO2 increase. The sensitivity of the obliquity-dependence to these threshold values has been investigated for growth rate threshold values ranging from 1 to 2.2 ppm/century, and 3 to 11 ppm for the threshold related to the $CO_2$ increase amplitude (Supplementary Figure 8, Supplementary Table 4). The dependence of CDJ occurrences to the obliquity context remains strong regardless of the threshold values used (Supplementary Figure 8). Nevertheless, the proportion of high-obliquity CDJs increased with the absolute value of the thresholds. The proportion reaches 100% for a 2.2 ppm/century threshold or a 11 ppm one (5/5 and 7/7 CDJs, respectively). The result of this test underlines than the most pronounced centennial-scale $CO_2$ variations are dependent to the obliquity context, regardless of the threshold values considered to define the CDJs.

**Context of occurrences of the identified CDJs**

We compiled ten CDJ+ that occurred synchronously to a large atmospheric $CH_4$ increase, including two new ones identified in this study, which are a potential consequence of a DO-like event (Supplementary Figures 3 and 4, Supplementary Table 1). Oceanic circulation changes associated with some DO events induced a centennial-scale response of the carbon-cycle characterized by a 5 to 10 ppm $CO_2$ increase as measured in Antarctic ice cores [9–11]. This response is due to major climatic perturbations in the Northern Hemisphere and the tropics, including a northward shift of the Intertropical Convergence Zone (ITCZ) that induced the formation of new tropical wetlands [12].

Reversely, ten of them are considered as CDJ- as they are associated with a potential HE without major $CH_4$ increase and can be associated to an IRD peak in the oceanic record (Supplementary Figure 3 and 4). During the HS, an ITCZ shift is evidenced in $CH_4$ at the time of the rapid $CO_2$ increase and following ref. [12], we interpret this as being related to further reduction/shutdown of the AMOC while its intensity during a stadial is already reduced. The shutdown with the HS is thought to cause a moderate increase of $CH_4$ of less than 50 ppb [11]. However, the fact that CDJs- are not systematically associated with a $CH_4$ increase was already observed in older parts of the EDC ice core [9]. It could be explained by the gas diffusion in the deepest part of the ice core or by the insufficient resolution of the $CH_4$ record (Fig. 1, Supplementary Figure 1), which is also limited by the width of the gas age distribution in the ice core samples [9].

Finally, two CDJs are not directly related to an IRD peak or a large atmospheric $CH_4$ increase. Consequently, we consider these two CDJs as unclassified and refer to them as CDJ 7b and CDJ 7c.

**Impact of the choice of ice core chronologies on absolute CDJ dating**

In this study, we display our ice-core record onto the AICC2023 chronology [13] which is the new chronology of reference for the EDC ice core. This chronology is based on a Bayesian dating tool that combines different chronological constraints (e.g. $\delta^{18}O_{atm}$, $\delta O_2/N_2$ and total air content records). The average uncertainty over the last 500 ka is 0.9 ± 0.4 ka for the AICC2023 gas chronology. The period of highest uncertainty, excluding the last meters of the ice core, occurs over the 450-350 ka period reaching up to ~2 ka. Two other EDC ice core age-scales have been used over the past years: the AICC2012 [14,15] and the $\delta^{18}O_{calcite}$ chronologies [16]. The AICC2012 chronology was the ice core chronology of reference of the past decade and was built using a probabilistic model combining different chronological constraint. The $\delta^{18}O_{calcite}$ chronology relies on the assumption of a strong covariation of the $\delta^{18}O$ record from East-Asian speleothems with the $\delta^{18}O_{atm}$ measured in the gas phase of the EDC ice core. The $\delta^{18}O_{calcite}$ chronology is a compromise between AICC2012 age markers and speleothem-based alignment. The largest age difference between the three chronologies is found during the 440-350 ka period, reaching ~4 ka [16]. This 4-ka difference in the assignment of absolute ages could lead to a change of up to 0.5° in their respective obliquity values This large dating uncertainty over this interval is illustrated in Supplementary Figure 7. Despite this multi-millennial-scale discrepancy between the three chronologies, the chi-square test led to the rejection of the null hypothesis for all of the chronologies: (i) for AICC2012, the null hypothesis of an independence of CDJ occurrence from the obliquity state could be rejected at 95% of confidence. (ii) for the $\delta^{18}O_{calcite}$ and the AICC2023 chronologies, the chi-square test rejects this null hypothesis at 90% of confidence (Supplementary Table 2). We also test the influence of the choice of the orbital parameter data sets by comparing the one from ref. [17] and from ref. [18] (Supplementary Figure 7). The results confirms the absence of a dating-dependence of our results, as 18 of the 22 CDJs occurred above the mean obliquity value of the 12 obliquity cycles of the last 500 ka when the astronomical solution from ref. [18] and the AICC2023 chronology is considered.

**Climatic impact of a low obliquity state**

A change of the obliquity value induces a change in the repartition of the solar energy at the surface of the Earth. Especially, a lowering of the obliquity value will induce a reduced insolation at the high latitudes. Consequently, a low obliquity state in experiment *LowOblCTR* leads to colder conditions at both northern and southern high latitudes compared to the control 49 ka experiment, which was done with the “realistic” obliquity at 24.3° (Fig. 4a). The mean air temperature anomaly is -4.2°C north of 60°N (Supplementary Figure 18). The cooling extends to the mid-latitudes, particularly over the continental areas. The high-latitude cooling is associated with a 7 % and 9 % increase in annual mean sea-ice cover in the Northern Hemisphere and the Southern Ocean, respectively. The resulting enhanced temperature gradient between the poles and the tropics impacts the hydrological cycle,

shifting the ITCZ southward as well as inducing drier conditions at mid to high latitudes (Fig. 4b). These climatic changes impact the vegetation and soil carbon, with widespread decrease of the terrestrial carbon content, but more particularly in the northern high latitudes, the Sahel Zone and the Middle East. As a result, the terrestrial carbon reservoir is 105 GtC (7%) lower in *LowOblCTR* than in *HighOblCTR*.

**Climatic response to a North Atlantic meltwater input**

The meltwater addition of 0.3 Sv into the North Atlantic leads to an AMOC shutdown in ~300 years in all experiments. The AMOC stays completely off during the duration of the meltwater pulse (i.e. until year 1000), after which it slightly increases to 5 Sv, before abruptly recovering between years 1800 and 2000 as salt is added to the North Atlantic. The AMOC shutdown leads to a reduced meridional oceanic heat transport to the North Atlantic, and therefore to a 7°C reduction in Sea Surface Temperatures (SST), as well as sea-ice advance, in the North Atlantic [19]. This leads to an atmospheric cooling over most regions north of the equator apart from the north-eastern Pacific (Fig. 4a). The warming over the north-eastern Pacific is due to enhanced North Pacific Intermediate Water formation [20,21].

The reduced meridional oceanic heat transport to the North Atlantic leads to an SST increase in the South Atlantic, that is spreads into the Southern Ocean through the Antarctic circumpolar current, (+1.6°C, zonal average over 45-60°S obtained 400 years after the beginning of the meltwater addition). These temperature changes impact the hydrological cycle (Fig. 4b, Supplementary Figure 18), with notably drier conditions over Europe, North Africa and the western part of Asia. In addition, a southward shift of the Intertropical convergence zone is simulated, thus leading to drier conditions in the northern tropics and wetter conditions in the southern tropics [19].

**Choice of the 400 yr timing to compare low and high obliquity simulations**

Fig. 3b shows the evolutions of the $\Delta CO_2$ from the different simulations performed in this study over the 800 years following the AMOC shutdown. Here we propose a quantitative approach to estimate the centennial-scale response time of the carbon cycle to the AMOC perturbation. To do so, we apply the linear fit model based on a least square approach [22] to determine objectively slope breaks in the atmospheric $\Delta CO_2$ record from the reference *HighObl* simulation (Supplementary Figure 9). We choose the $CO_2$ output from the *HighObl* simulations because it is not affected by any artificial testing (e.g. low obliquity value, muted terrestrial vegetation, enhanced SHW). The change in slope, corresponding to the expected timing of the centennial to multi-centennial scale response of CDJ, is identified at 354 ±10 after the AMOC shutdown. Hence, it appears reasonable to consider that the total centennial-scale response to the AMOC shutdown is completed at ~400 yr.

**Vegetation and carbon cycle response to an AMOC shutdown**

These climatic changes impact the vegetation cover and the soil carbon, with a reduction of carbon stored in most of the northern hemisphere, particularly at high northern latitudes (-53 GtC, for *HighObl*) and in the northern tropics (-53 GtC, for *HighObl*), while there is an increase in the southern tropics (+35 GtC, for *HighObl*). Overall, there is a 70 GtC loss from the terrestrial biosphere in *HighObl*, mostly occurring during the first 400 years of the simulation (Supplementary Figure 8).

Since the climate is colder and the precipitation pattern altered in the control experiment under a low obliquity state, the terrestrial carbon reservoir is 105 GtC lower (Fig. 4). As a result, the terrestrial biosphere only loses 34 GtC in *LowObl*.

A previous study has shown that the AMOC shutdown and associated changes in oceanic circulation lead to a large reorganisation of dissolved inorganic carbon (DIC) concentration in the ocean [23]. Due to the reduction of the North Atlantic Deep Water transport, the carbon content in the Atlantic basin (north of 35°S) increases by 250 GtC in *HighObl*, and 245 GtC in *LowObl* (Supplementary Figure 19).

Due to slightly higher stratification and increased DIC within the Atlantic water masses, the Southern Ocean carbon reservoir increases by 60 GtC in *HighObl* and 42 GtC in *LowObl* (Supplementary Figure 19). However, as the North Pacific Intermediate Water flow increases to up to 30 Sv, there is large carbon decrease in the Pacific basin (-270 GtC in *HighObl* and -282 GtC in *LowObl*) (Supplementary Figure 19).

If the terrestrial carbon fluxes are muted, the Southern Ocean carbon increase is reduced (+40 GtC in *HighObl_NoVeg* and +37 GtC in *LowObl_NoVeg*), while the decrease in the Pacific basin is enhanced (-294 GtC in *HighObl_NoVeg* and -284 GtC in *LowObl_NoVeg*).

In the experiments where a strengthening of the SH westerlies is imposed, enhanced upwelling of DIC-rich deep waters leads to a $CO_2$ outgassing in the Southern Ocean. The stronger ventilation in the Southern Ocean reduces the DIC concentration in the Southern Ocean and within Antarctic intermediate waters [24] (Supplementary Figure 19). Consequently, the carbon reservoir increase is reduced in the Southern Ocean (20 GtC in *HighObl_SHW* and 4 GtC in *LowObl_SHW*), and in the Atlantic (i.e. 238 GtC in *HighObl_SHW* and 235 GtC for *LowObl_SHW*). The loss of carbon from the South Pacific is also accentuated, while it is attenuated in the North Pacific due to increased southern sourced waters. As a result, there is an accentuated loss of carbon from the Pacific in *HighObl_SHW* (-282 GtC), while the loss of carbon is attenuated in *LowObl_SHW* (-252 GtC) (Supplementary Figure 19).

**CDJ+ simulations at 12 ka**

As a result of the meltwater input in YDNA and YDlowOblNA, the AMOC weakens from 20 Sv to 13 Sv in both experiments. After 1000 years, the meltwater input is stopped, so that the AMOC recovers in 150 years in YDNA and 100 years in YDlowOblNA. The simulated atmospheric $CO_2$ evolution is similar in both experiments with a 7 ppm slow decrease during the AMOC shutdown, a rapid 4ppm $CO_2$ decrease during the first 90 years of the AMOC recovery, and a 8 ppm $CO_2$ increase during the following 400 years (Supplementary Figure 21).

In both experiments, the atmospheric $CO_2$ increase during the AMOC recovery phase is due to an oceanic carbon release of 60 GtC, while the terrestrial carbon content increases by 55 GtC (Supplementary Figure 21). The faster rate of terrestrial carbon increase than the rate of oceanic carbon release during the first 85 years of the AMOC recovery leads to the transient atmospheric $CO_2$ decrease. The larger rate of oceanic carbon release than terrestrial carbon uptake after that leads to the atmospheric $CO_2$ increase. The oceanic carbon release is due to a deep ocean DIC decrease. The DIC decrease is maximum in the deep North Atlantic and results from the NADW re-invigoration (Supplementary Figure 22). The DIC decrease in the deep Indo-Pacific results from enhanced Antarctic Bottom Water transport. The deep ocean DIC decrease is however partially compensated by a DIC increase in the top 1500m (Supplementary Figure 22). In addition, the CDJ+ experiments under low and high obliquity here provide a similar result, even though as in the CDJ- experiments the terrestrial carbon changes are smaller under low than high obliquity.

**Comparison with anthropogenic-induced $CO_2$ emissions**

The typical amplitude and increase rate for past CDJ events is ~10 ppm at a growth rate of ~7 ppm/century ref. [9]. The largest CDJ is registered at the end of Termination IV at 335 ka, it corresponds to a $CO_2$ concentration rise of 15.8 ppm in ~60 years. Since 1850, the anthropogenic activities have caused an atmospheric $CO_2$ increase of ~140 ppm which is nine times larger. The atmospheric $CO_2$ increase rate during this CDJ at the end of TIV is equivalent to an increase rate of atmospheric $CO_2$ concentrations of 26.2 ppm/century. If we consider the 1960-2022 period, the average increase rate of atmospheric $CO_2$ concentrations is 160 ppm/century. Hence, this is six time larger than the growth rate of the most intense CDJ. Thus, the centennial-scale variability of carbon cycle described in this

study is not of the same order of magnitude than the current anthropogenic emissions however, we illustrate below that this is not negligible.

Over the 2010-2019 period, the average emission rate of anthropogenic $CO_2$ is 40 ± 4.3 $GtCO_2.yr^{-1}$ (IPCC 2022 AR6, WG1). Of this total, only 46 % remains in the atmosphere (IPCC 2022 AR6, WG1). Consequently, the atmospheric $CO_2$ concentrations increase by 2.4 ± 0.3 $ppm.yr^{-1}$ due to anthropogenic activity. We thus divided the average value of CDJ amplitude (10 ppm) by this value to obtain its equivalent in term of 2010-2019 anthropogenic $CO_2$ emission. The resulting value is 4.3 years of anthropogenic $CO_2$ emission based on the 2010-2019 average.

## Supplementary Figures

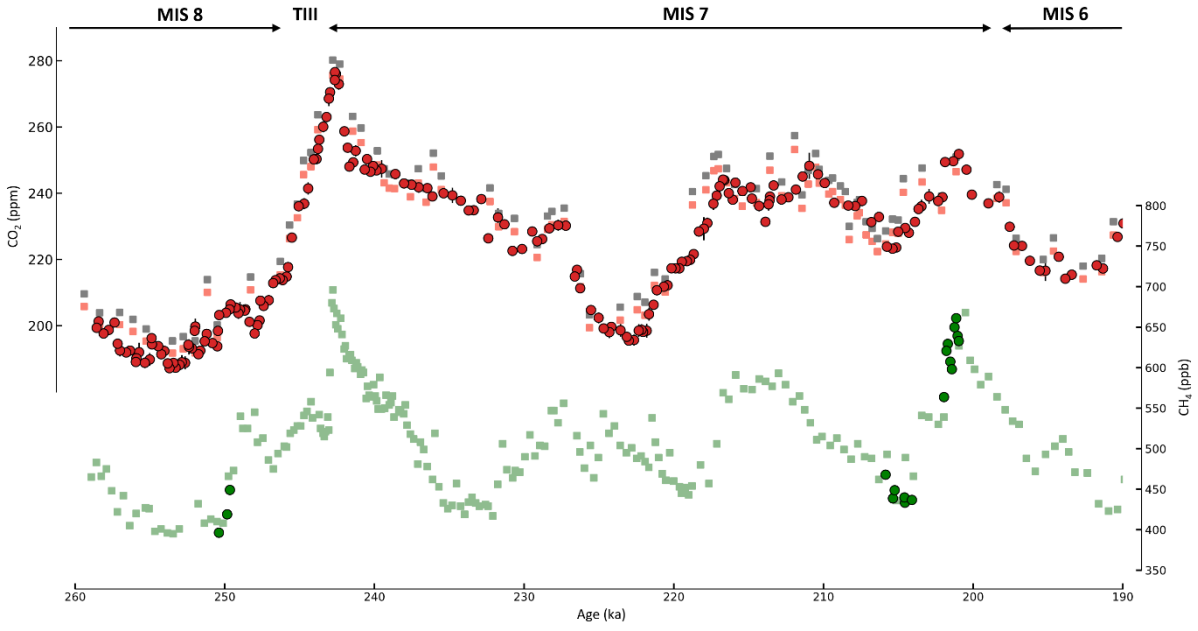


**Supplementary Figure 1: Published and new $CO_2$ and $CH_4$ measurements covering the 260-190 ka time-period.** (Top panel) New $CO_2$ measurements on the EDC ice core (red dots, this study). Error bars correspond to 1σ standard deviation computed as the quadratic sum of gravitational correction error, measurement system error and the standard deviation of the five injections (see methods). Published $CO_2$ data from the Vostok ice core [1] (grey squares) and Vostok $CO_2$ data corrected including gravitational and blank corrections (light red square, this study). All records are plotted on the AICC2023 gas timescale [13]. (Bottom panel) New (green dots, this study) and published [25,26] (light green squares) $CH_4$ records from the EDC ice core.

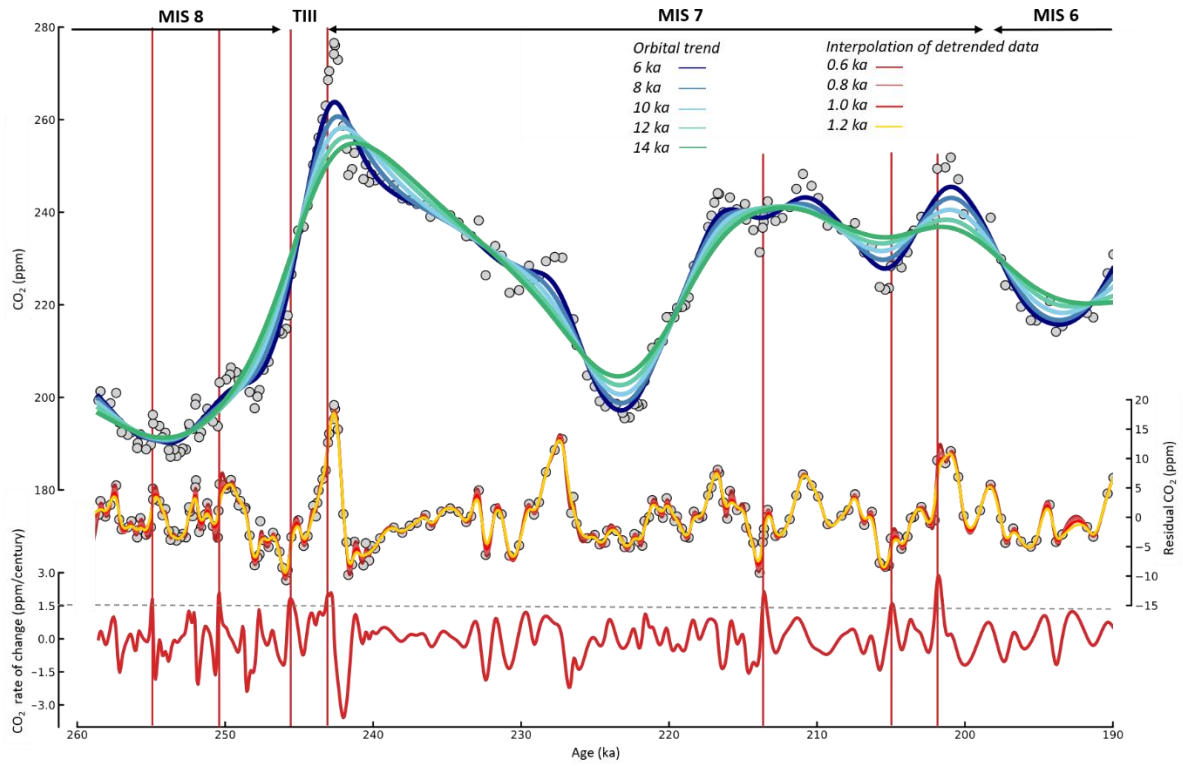


**Supplementary Figure 2: Calculation of the $CO_2$ rate of change across the 260-190 ka interval based on the new EDC $CO_2$ record**. Top: Orbital- to multi-millennial-scale trends from the EDC $CO_2$ record (grey dots, this study) using five different smoothing splines [27] with cut-off periods (i.e., degrees of smoothing) ranging from 6 to 14 kyr. Middle: Detrended EDC $CO_2$ record after subtraction of the 10 kyr spline. A second set of five smoothing splines with cut-off periods ranging from 0.6 to 1.2 kyr is applied to the 10 kyr-detrended data set. Bottom panel: Resulting rates of change of the detrended $CO_2$ record for the 1.0 kyr smoothing spline [9]. Vertical red lines indicate the timing of the identified CDJs. A centennial-scale $CO_2$ release is identified when the rate is higher than 1.5ppm/century (dashed horizontal line) [9].

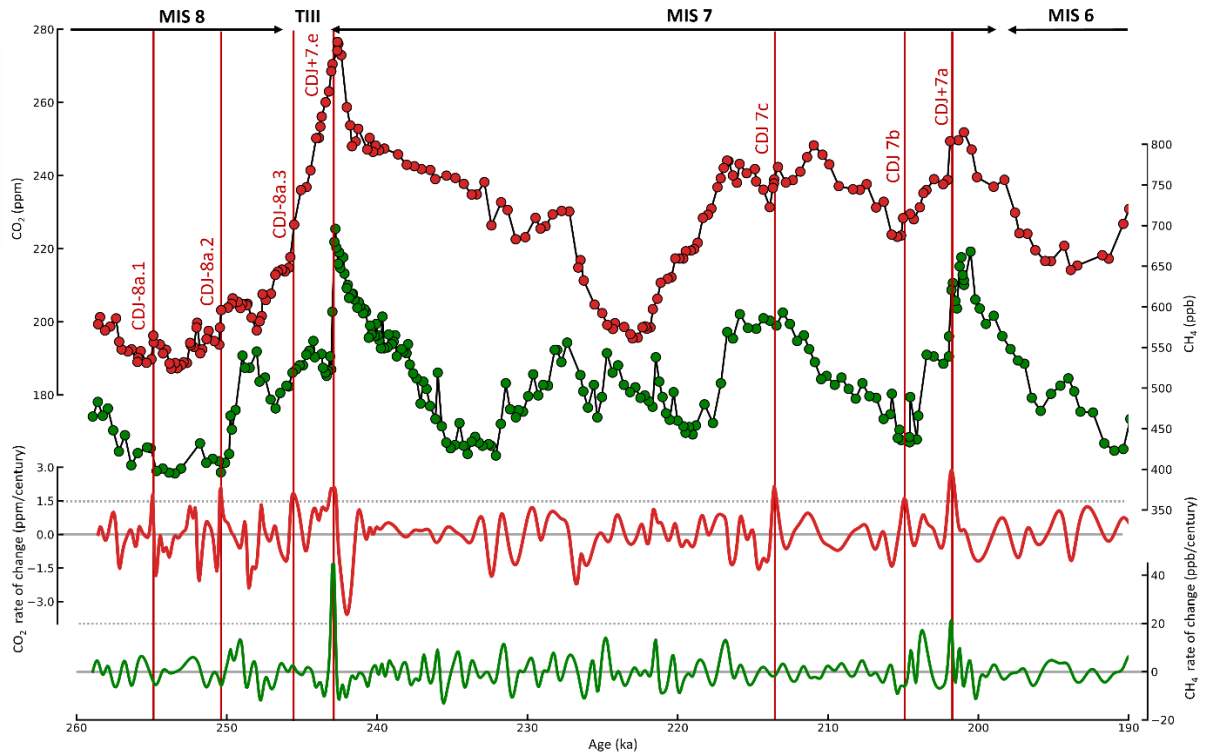


**Supplementary Figure 3: Identification of centennial-scale CDJs between 260 and 190 ka.** Top: EDC $CO_2$ record on (red dots, this study). Middle: EDC $CH_4$ record (green dots, this study and ref. [25,26]). Bottom: Resulting rates of change of the detrended $CO_2$ and $CH_4$ records for the 1.0 ka smoothing spline. Vertical red lines indicate the timing of the identified CDJs. A centennial-scale $CO_2$ release is identified when the rate is higher than 1.5 ppm/century (dashed horizontal line) [9] and a minimum amplitude of 5 ppm is registered. It is considered to be associated with a significant $CH_4$ increase (CDJ+) when the $CH_4$ rate of change is higher than 20 ppb/century. All records are on the AICC2023 timescale [13]. The nomenclature of CDJ follows the one from ref. [9] and is based on five components: 1. CDJ : carbon dioxide jump; 2. + or - : referring to the occurrence of synchronous massive $CH_4$ release (+) or not (-); 3. A number, referring to the corresponding Marine Isotopic Stage; 4. A letter, when the corresponding Marine Isotopic Stage have been subdivided into substages; 5. A number, in case the CDJ is not the only one occurring in the substage.

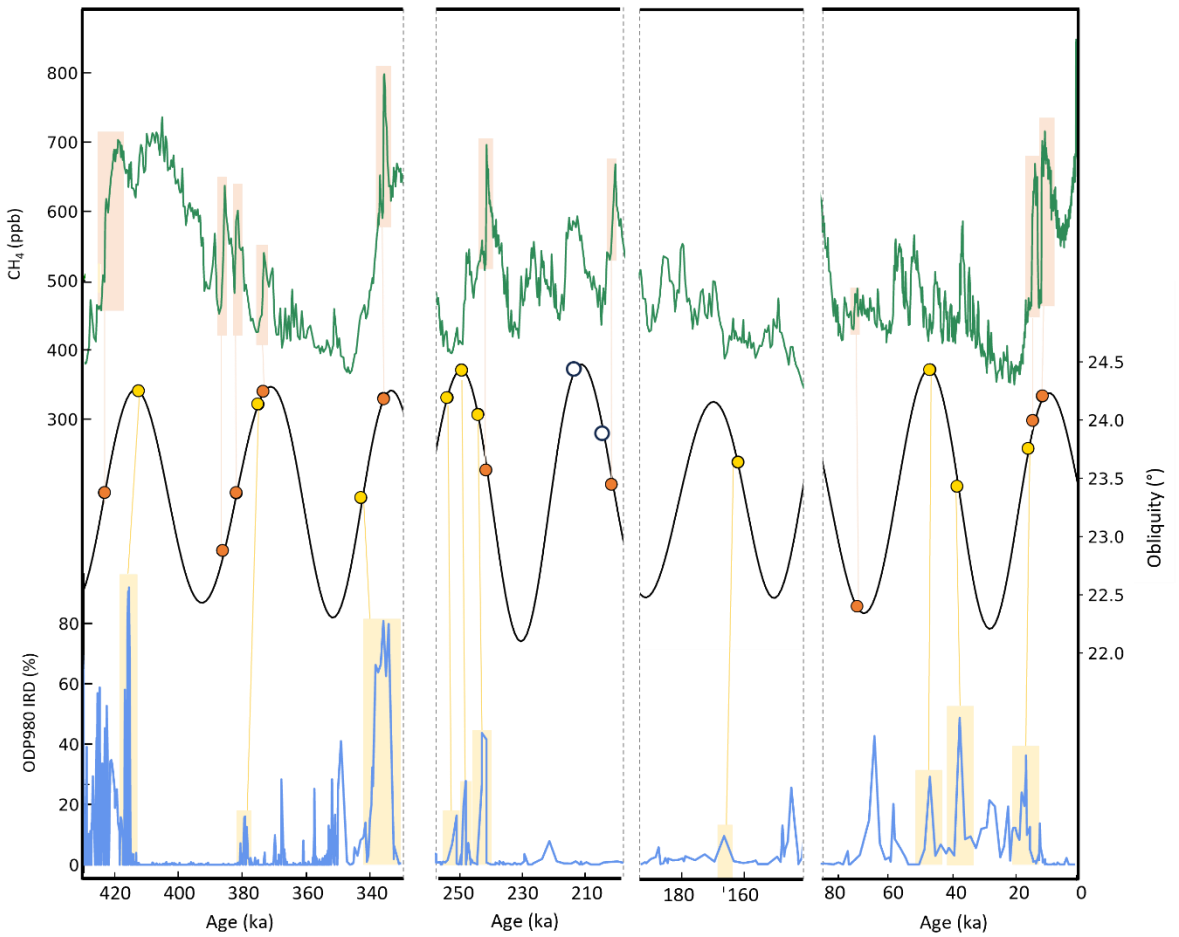


297

298

299 **Supplementary Figure 4: Identification of DO-like and Heinrich-like events associated with CDJs over the last**
300 **500 ka.** Top: atmospheric $CH_4$ record from the EDC ice core [25] (top, green). Middle: Obliquity (middle, black). Dots
301 represent CDJs associated with Heinrich-like (yellow, CDJ-), DO-like events (orange, CDJ+), and two CDJs that
302 cannot be classified unambigously (white) this study and refs. [9–11,28–30]. Bottom: IRD record from the marine
303 sediment core ODP 980 on its original timescale [31] (bottom, blue). Yellow/orange shaded areas correspond to
304 Heinrich-like / DO-like events potentially associated with a CDJ.

305

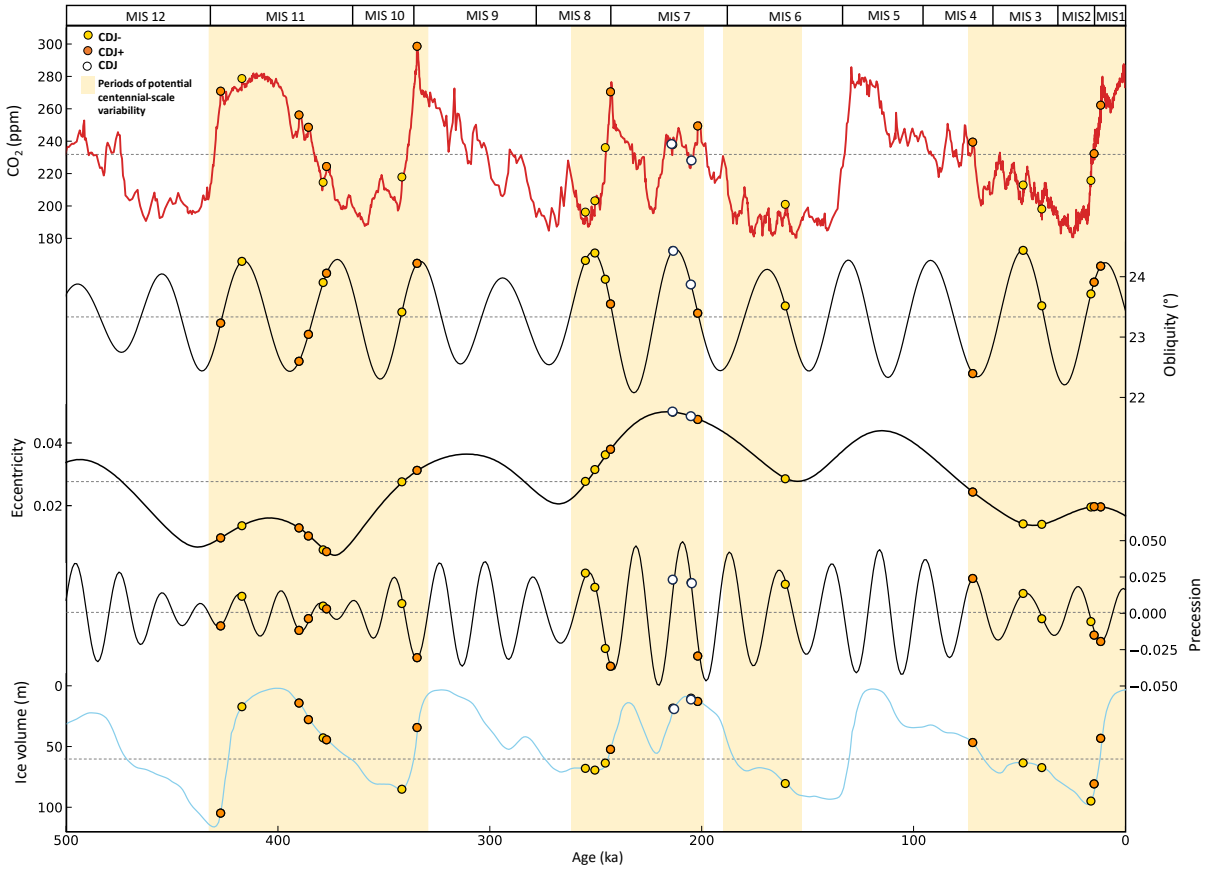


306

307 **Supplementary Figure 5: Orbital-scale climatic background of occurrences of the CDJs.** From top to bottom:
308 EDC $CO_2$ record (red, this study and refs. [9,11,29,30,32–34]). Obliquity (black). Eccentricity (black). Climatic Precession
309 (black) [17]. Global ice volume reconstruction [35] (blue). Yellow, orange and white dots indicate the timing of the
310 CDJ-, CDJ+ and CDJ occurrences in the context of the superimposed curve. Yellow bars represent the time
311 intervals where the temporal resolution of the ice-core $CO_2$ records allows for the potential identification of
312 abrupt changes.

313

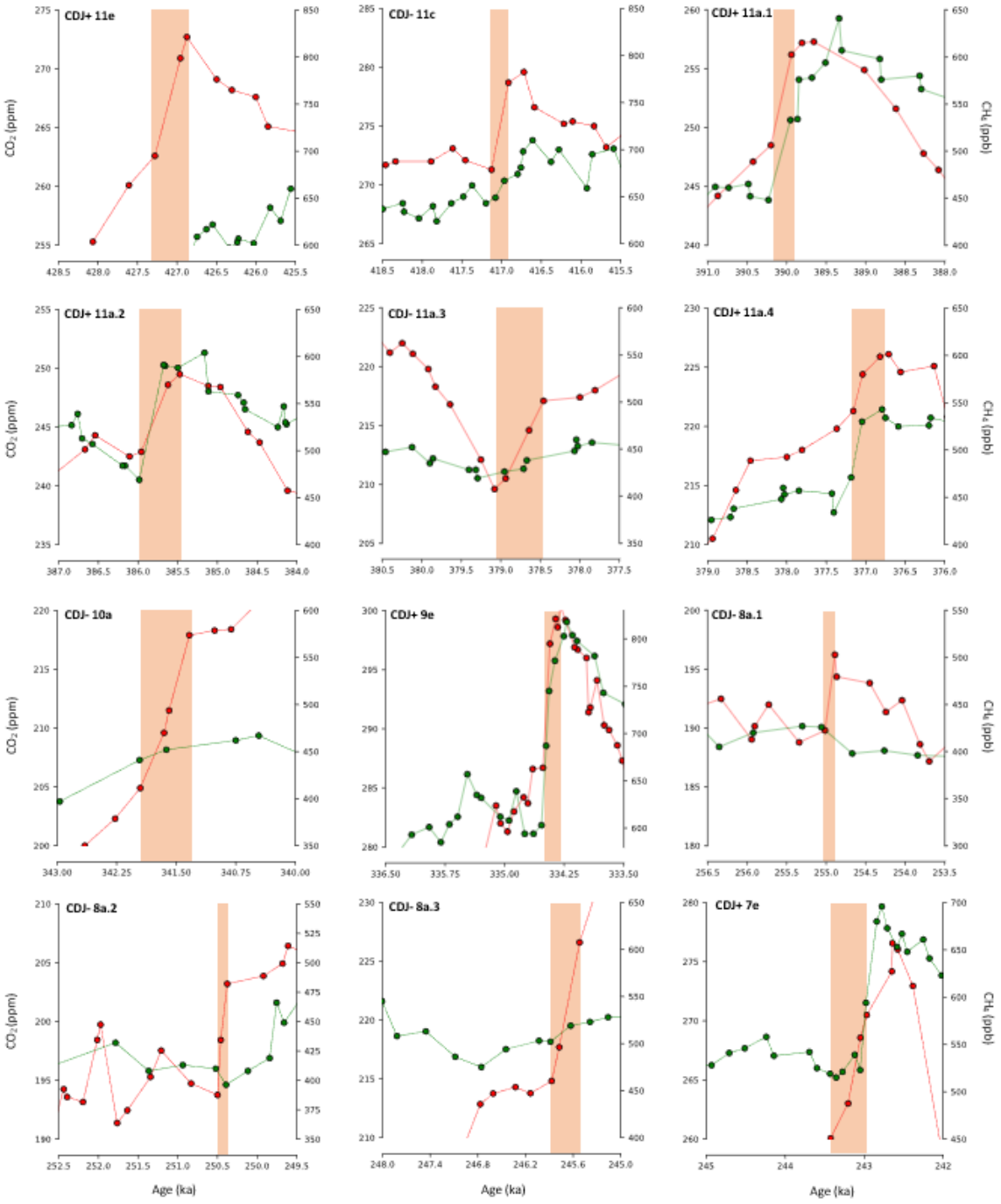


**Supplementary Figure 6: Detailed view of the 22 CDJs from the current and previously published studies.** EDC $CO_2$ (red line and dots) and $CH_4$ (green line and dots) records on the AICC2023 gas timescale [13] (older than 67 ka) and WD2014 [36,37] (younger than 67 ka) timescale (red dots). Vertical red bars correspond to periods associated with a CDJ.

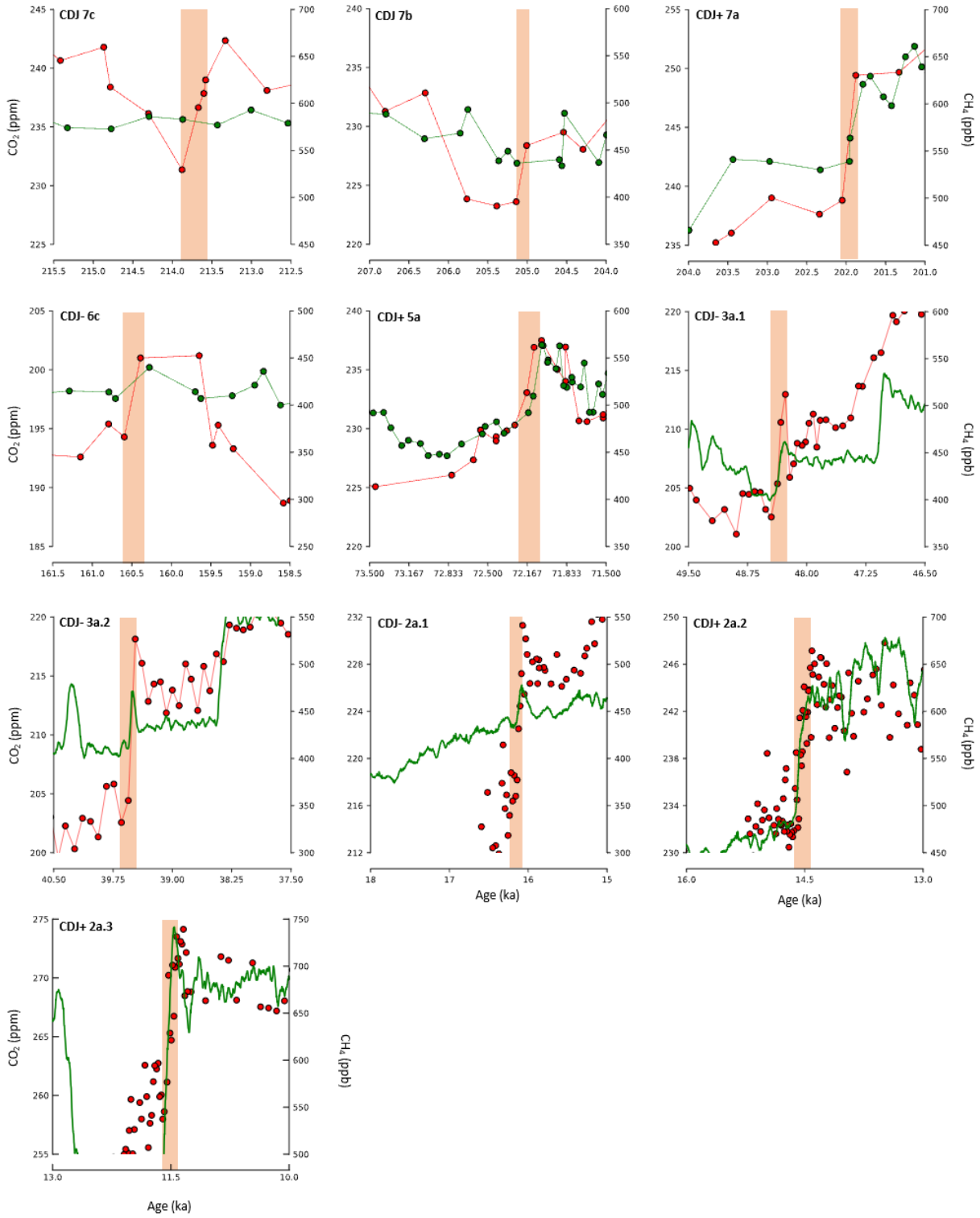


**Supplementary Figure 6 (continued).**

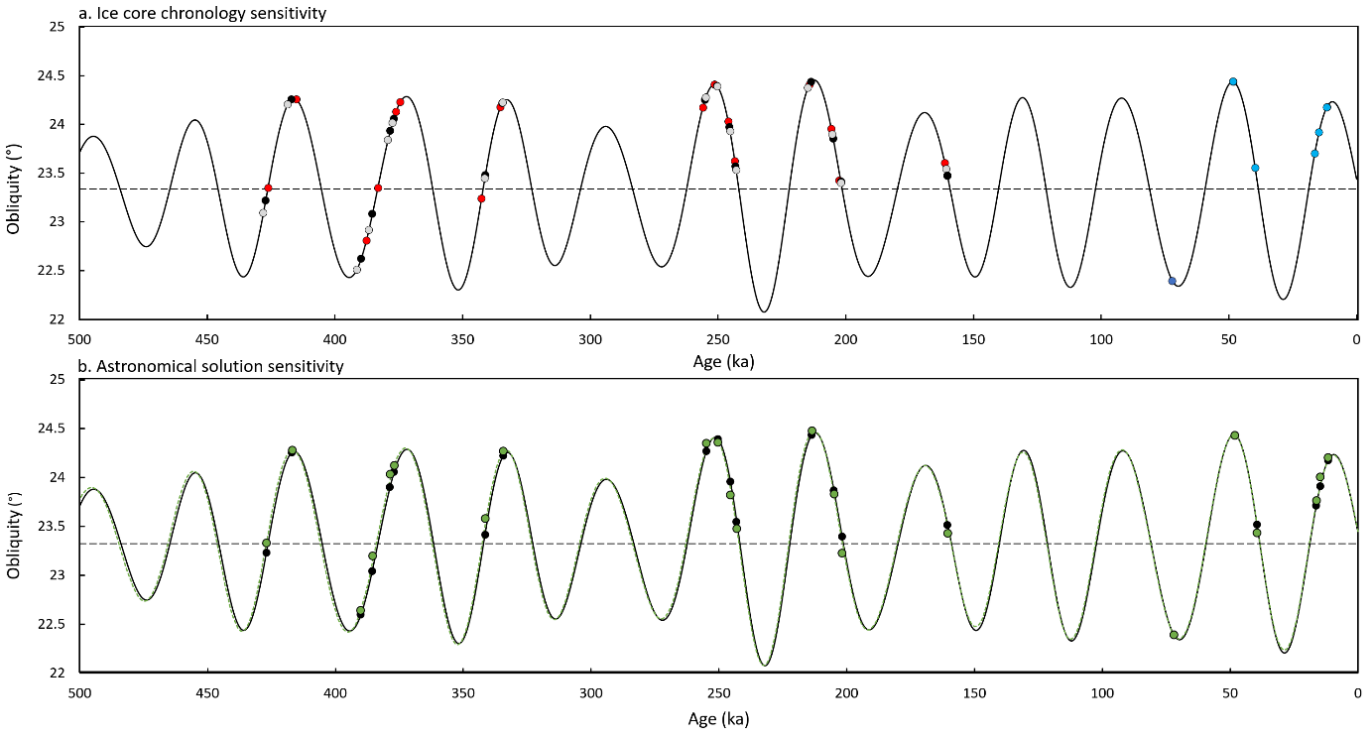


**Supplementary Figure 7: Testing the sensitivity of the relationship between the CDJs and the obliquity values to the choice of the ice-core gas chronology and of the astronomical solution. a.** : Dots correspond to CDJ occurrences put respectively on the WD2014 [36] (light blue), Taylor Glacier-adapted AICC2012 [30] (dark blue), AICC2023 [13] (black), $\delta^{18}O_{calcite}$ [16] (grey) and AICC2012 [14](red) ice core chronologies. **b.** Dots correspond to CDJ occurrences computed with the astronomical solution of ref. [17] (black) and ref. [18] (green), respectively. The ice core timescale used is AICC2023 [13] and Taylor Glacier-adapted AICC2012 [30] between 500 and 67 ka, and WD2014 [36,37] for the CDJs between 67 and 0 ka.

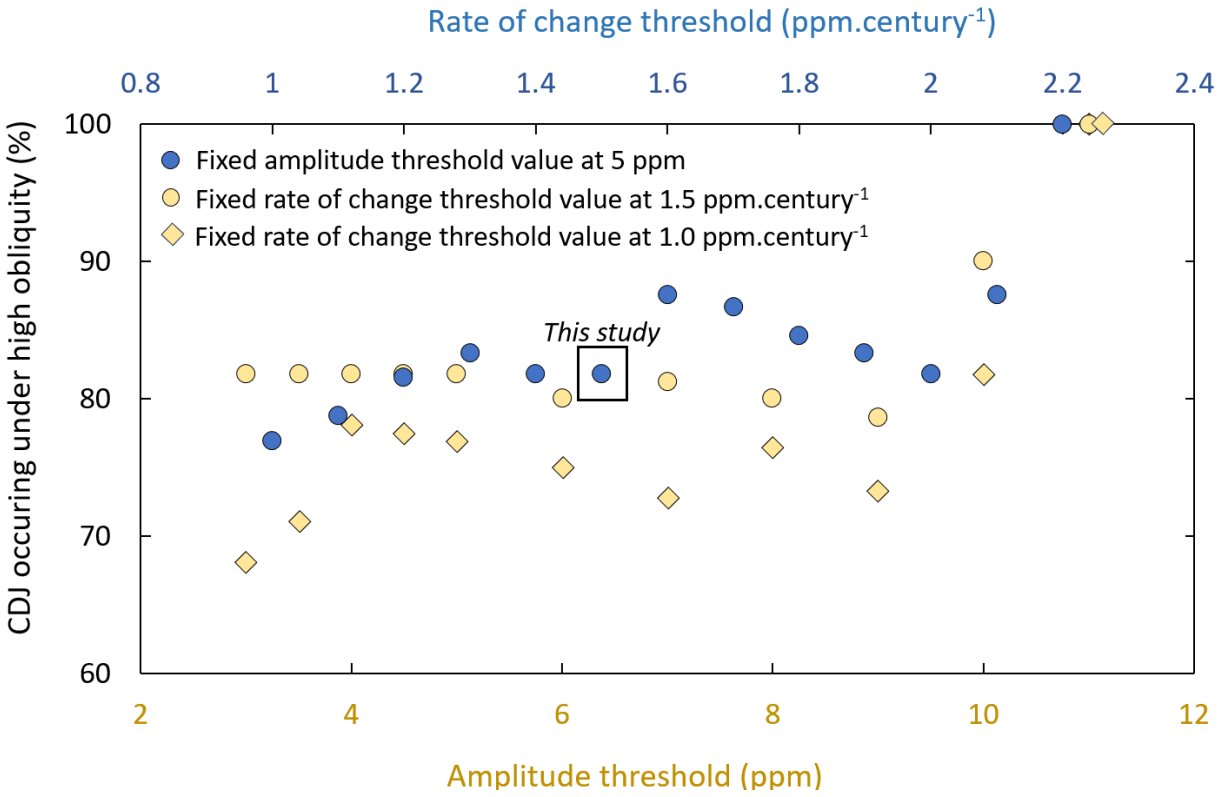


**Supplementary Figure 8: Testing the sensitivity of the link between the CDJs and the obliquity values to the choice of the CDJ detection threshold values.** Blue circles are the percentage of CDJs event occurring under high obliquity for a fixed amplitude threshold value of 5 ppm and various rate of change thresholds. Yellow circles/square are the percentage of CDJs event occurring under high obliquity for a fixed rate of change threshold value of 1.5/1.0 ppm.century$^{-1}$ and various amplitude thresholds. Note that above a certain threshold value, all CDJ events occurs under high obliquity. Detailed information on the identified CDJs are available in Supplementary Table 4. The threshold values of 5 ppm and 1.5 ppm.century$^{-1}$ applied in this study (black square) are the one defined in Ref. [9].

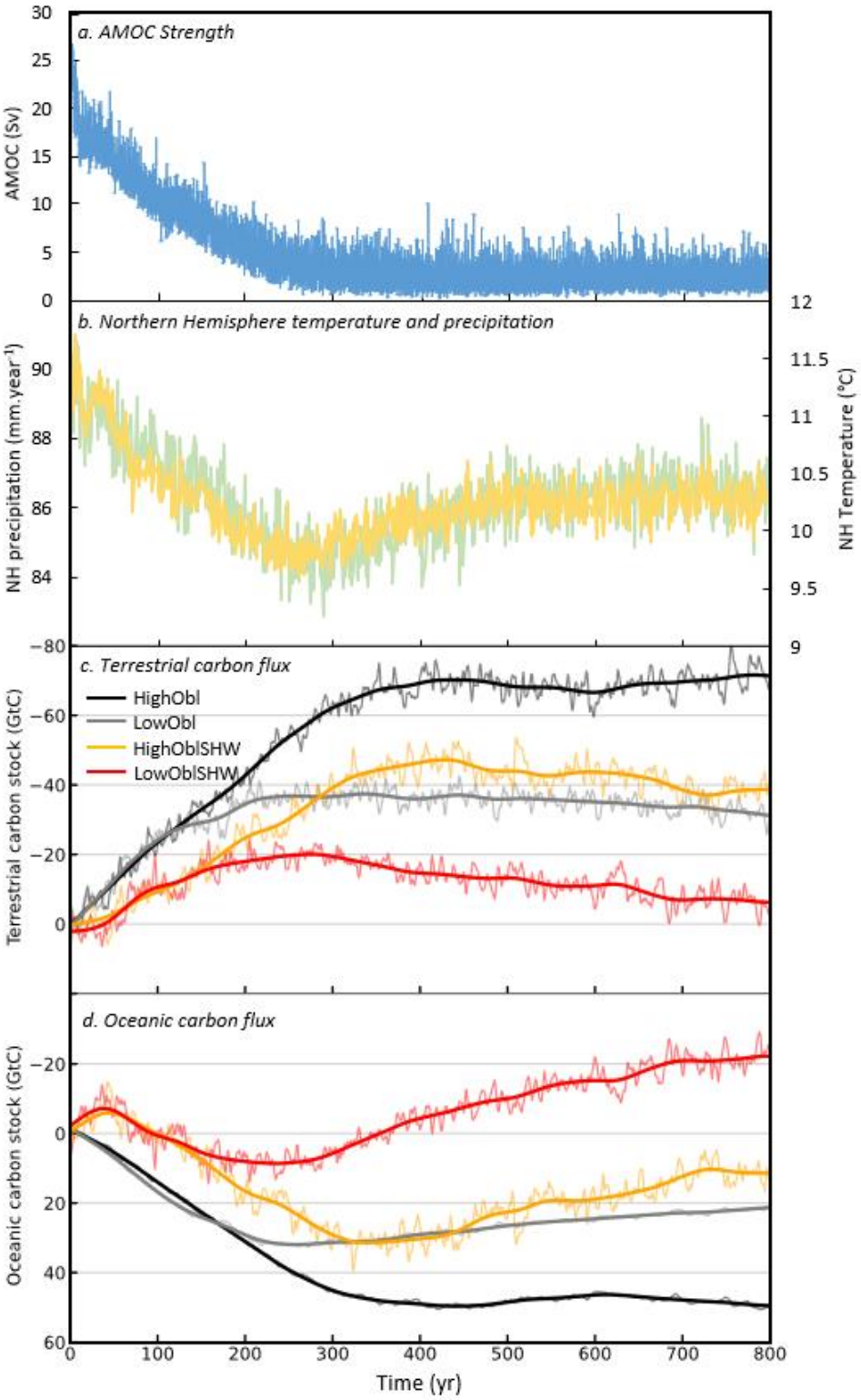


**Supplementary Figure 9: AMOC, climate, and terrestrial and oceanic carbon changes in carbon reservoirs during HS 5 under high and low obliquity phase. a.** Atlantic Meridional Overturning Circulation (AMOC) during the simulation. b. Average northern hemisphere temperature (yellow) and precipitation (green) during the simulation. c. Terrestrial carbon stock (in GtC) from the start of the simulation until 0.8 ka. *HighObl* and *LowObl* are performed under the obliquity at 49 ka (24.3°) and artificially low obliquity forcing (22.1°), respectively. *HighObl_SHW* and *LowObl_SHW* are similar to the previous two simulations with enhanced strength of Southern Hemisphere Winds (+20%). Bold lines are smoothing splines filters. d. Similar to c. but for oceanic carbon stock. The Y axis is reversed to show that a decrease in the terrestrial carbon leads to an atmospheric $CO_2$ increase.

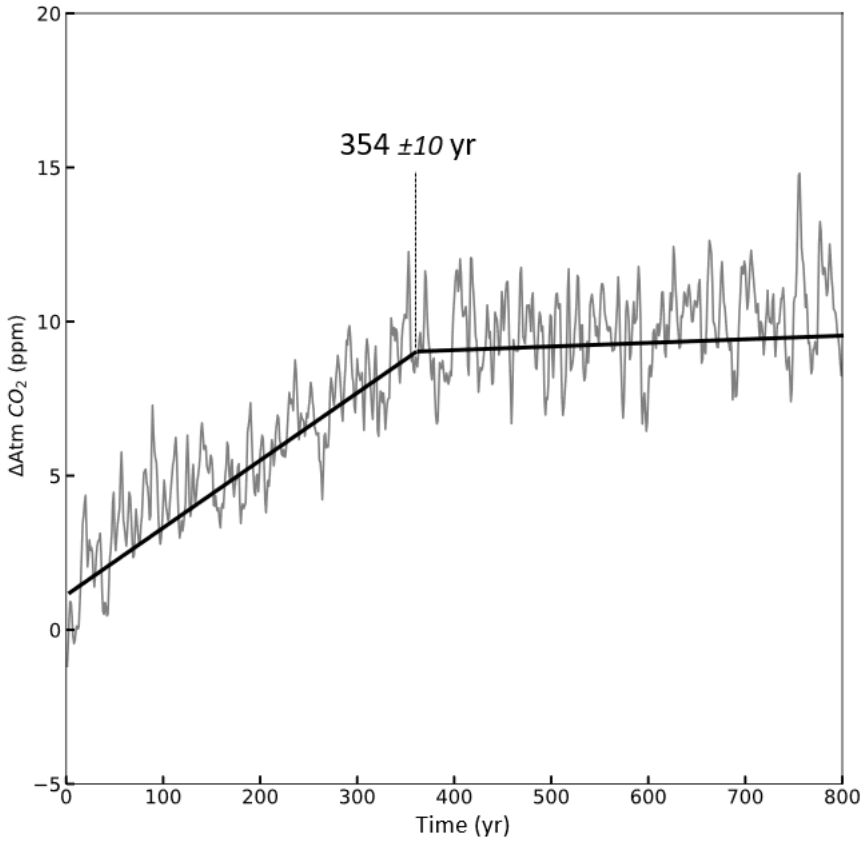


385

386 **Supplementary Figure 10:** Identification of slope break (black lines) of the simulated *HighObl* $\Delta CO_2$ (grey line)
387 using the LinearFit model [22].

388

389

390

391

392

393

394

395

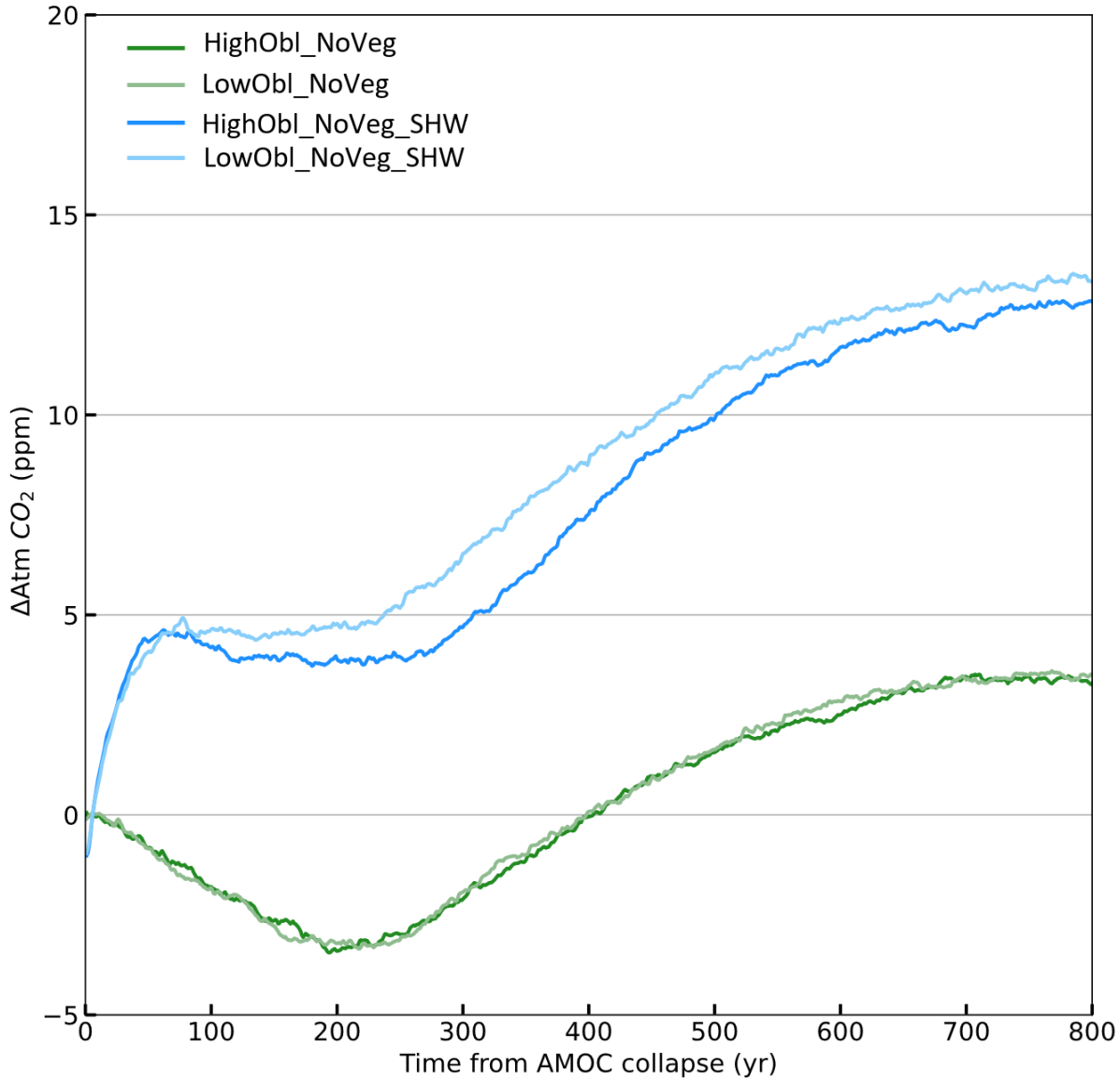


**Supplementary Figure 11: Simulating centennial-scale $CO_2$ changes during HS5 under high and low obliquity without terrestrial carbon fluxes.** Simulated $CO_2$ anomalies (ppm) for the first 800 years of the simulation. *HighObl_NoVeg* and *LowObl_NoVeg* are performed under the obliquity at 49 ka (24.3°) and artificially low obliquity forcing (22.1°), respectively. *HighObl_NoVeg_SHW* and *LowObl_NoVeg_SHW* are similar to the previous two simulations with stronger Southern Hemisphere windstress (+40%).

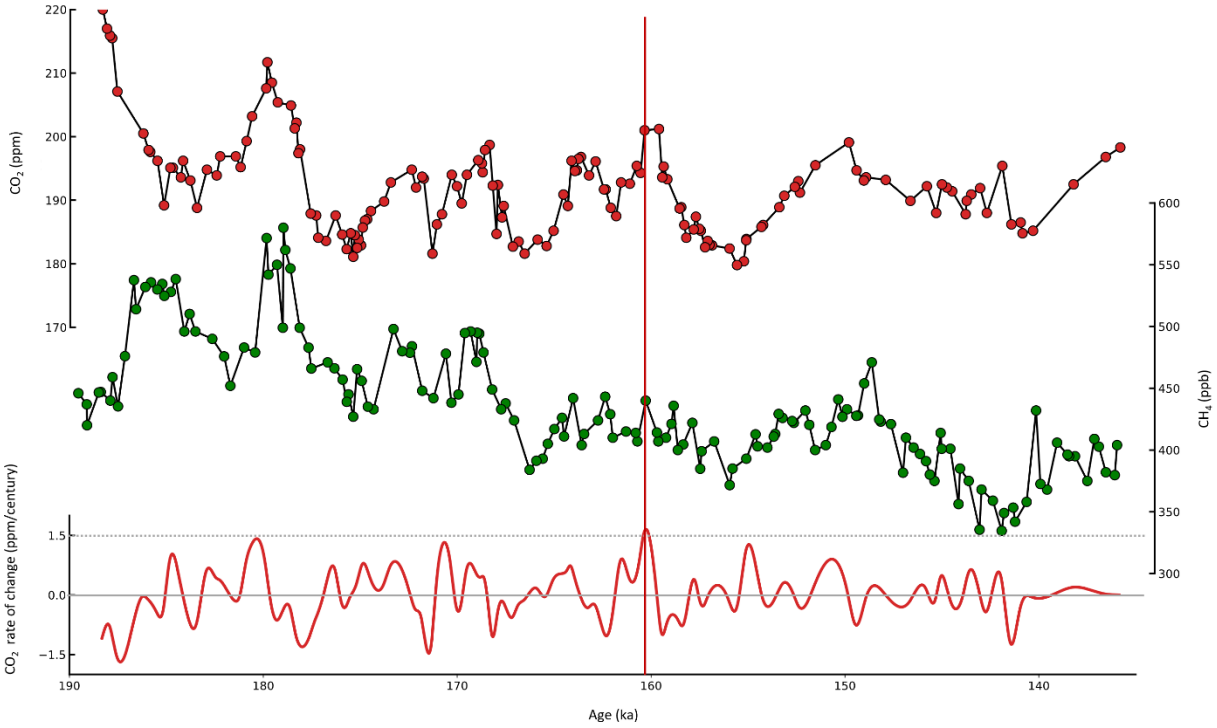


**Supplementary Figure 12:** Identification of centennial-scale CDJs between 190 and 135 ka. Top: EDC $CO_2$ record (red dots [29]). Middle: EDC $CH_4$ record (green dots [29]). Bottom: Resulting rates of change of the detrended $CO_2$ record for the 1.0 ka smoothing spline. Vertical red line indicates the timing of the identified CDJ. A centennial-scale $CO_2$ release is identified when the rate is higher than 1.5 ppm/century (dashed horizontal line) and a minimum amplitude of 5 ppm is registered.

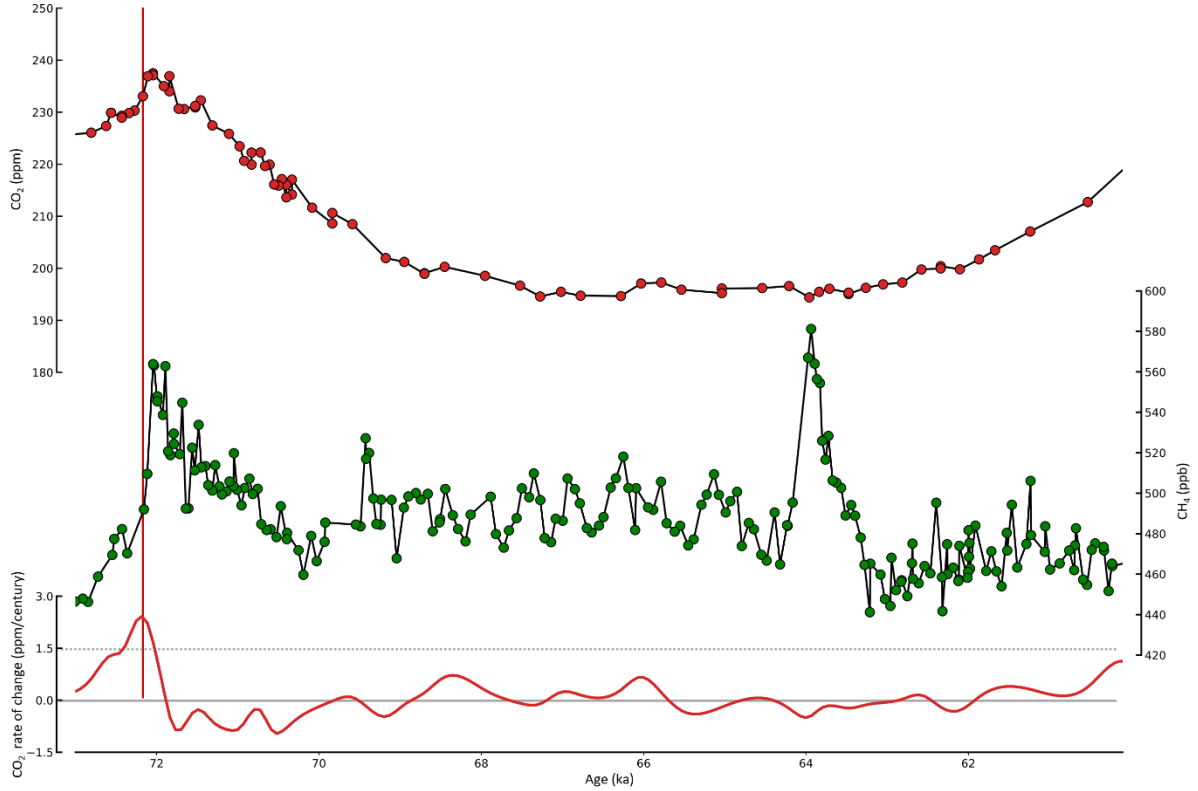


**Supplementary Figure 13:** Identification of centennial-scale CDJs between 75 and 60 ka. Top: Taylor Glacier $CO_2$ record (red dots [30]). Middle: EDC CH4 record (green dots [25]). Bottom: Resulting rates of change of the detrended $CO_2$ record for the 1.0 ka smoothing spline. Vertical red line indicates the timing of the identified CDJ. A centennial-scale $CO_2$ release is identified when the rate is higher than 1.5 ppm/century (dashed horizontal line) and a minimum amplitude of 5 ppm is registered.

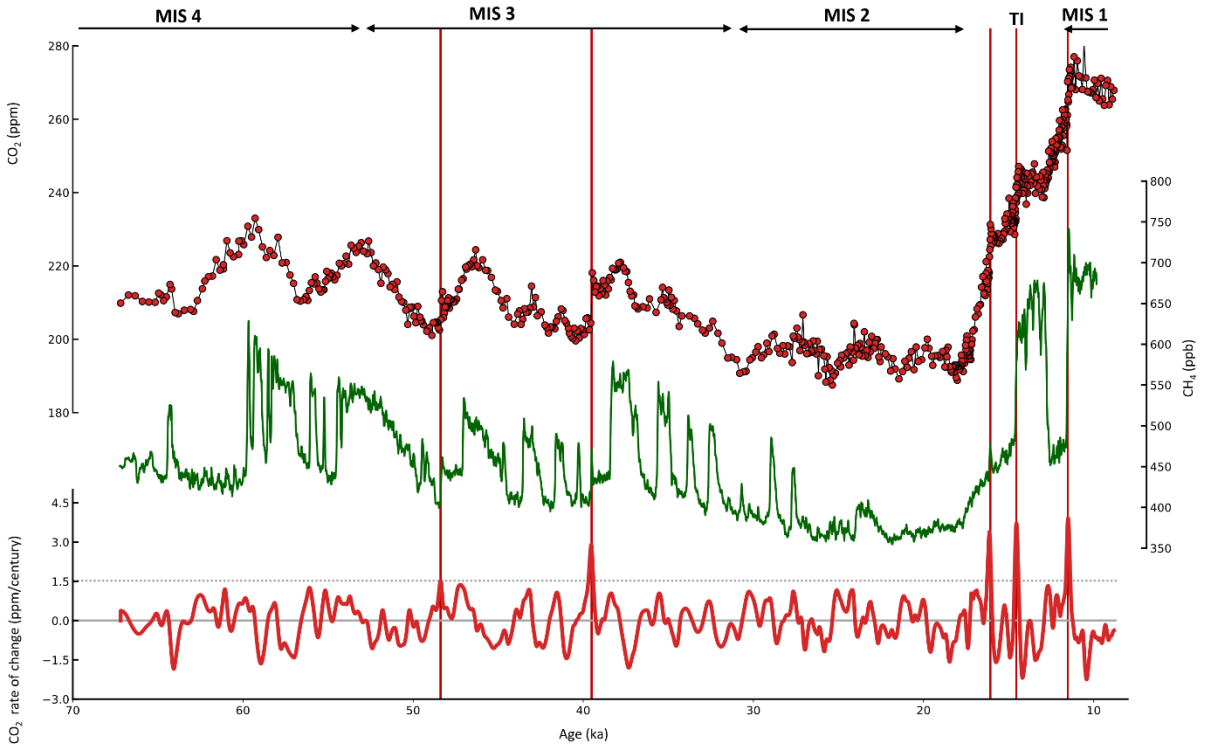


**Supplementary Figure 14:** Identification of centennial-scale CDJs between 60 and 8 ka. Top: WD $CO_2$ record (red dots [10,11]). Middle: WD $CH_4$ record (green dots [12]). Bottom: Resulting rates of change of the detrended $CO_2$ record for the 1.0 ka smoothing spline. Vertical red lines indicate the timing of the identified CDJs. A centennial-scale $CO_2$ release is identified when the rate is higher than 1.5 ppm/century (dashed horizontal line) and a minimum amplitude of 5 ppm is registered.

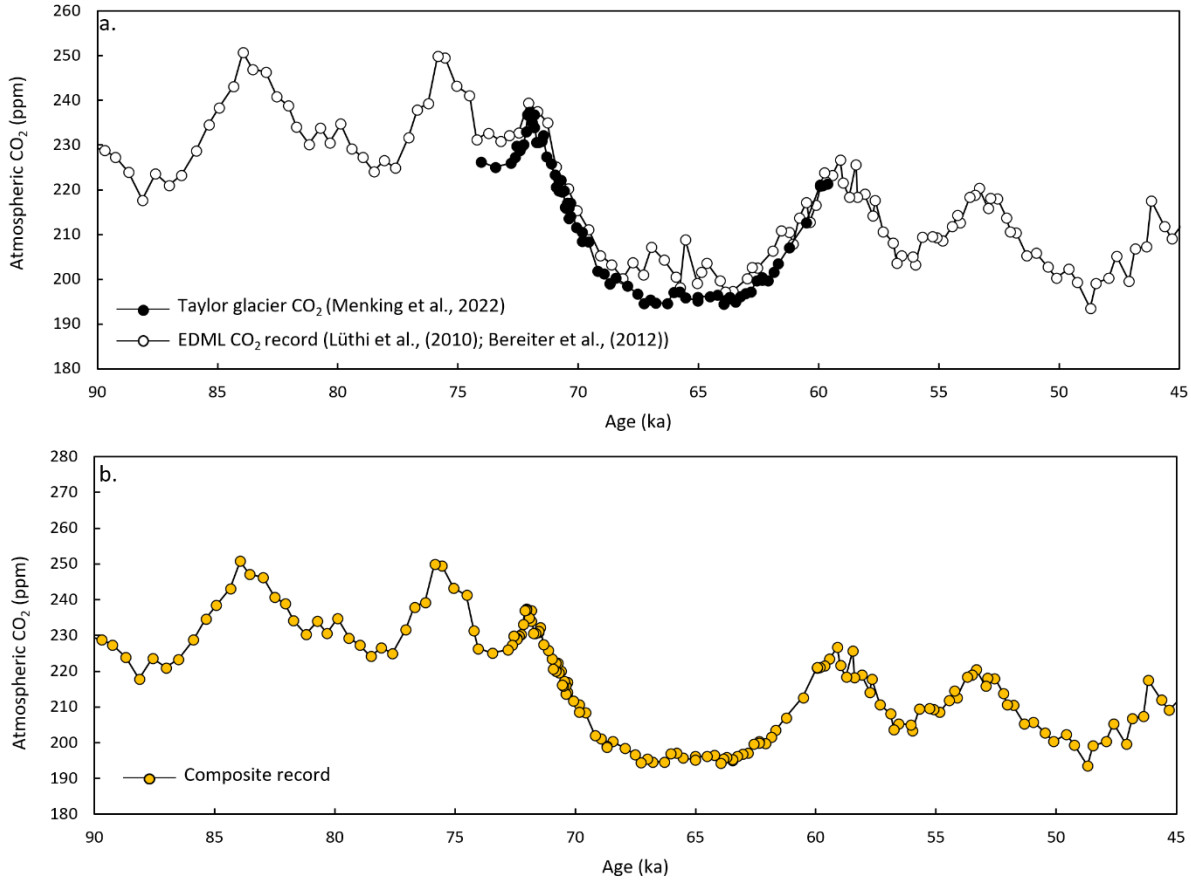


**Supplementary Figure 15:** a. High resolution $CO_2$ record from the Taylor Glacier [30] (75-60 ka) and millennial-scale $CO_2$ record from EDML [38,39] (90-45 ka) on the AICC2012 [14] and the Taylor Glacier -adapted AICC2012 derived [30] chronologies. b. Composite $CO_2$ record corresponding to the EDML (90-73 ka and 60-45 ka) and Taylor glacier (73-60 ka). Note that we only consider the CDJs identified across the Taylor Glacier segment of the $CO_2$ composite as the EDML segment is not resolved enough to allow a robust identification of CDJs.

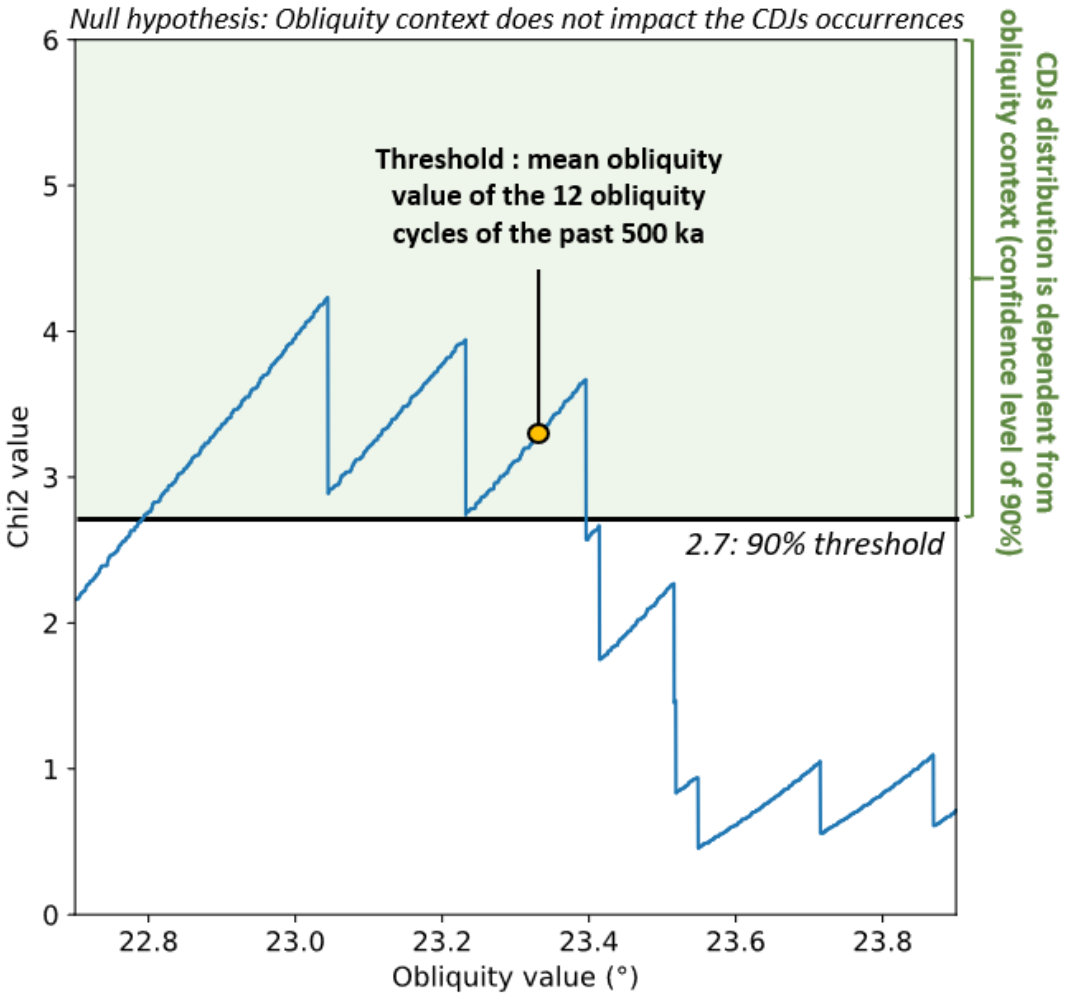


**Supplementary Figure 16: Sensitivity of the Chi-square test to the threshold obliquity value.** The null hypothesis is rejected at 90% of confidence when the Chi-square value (blue curve) is higher than 2.7. The expected value varies with the threshold of obliquity chosen (x-axis).

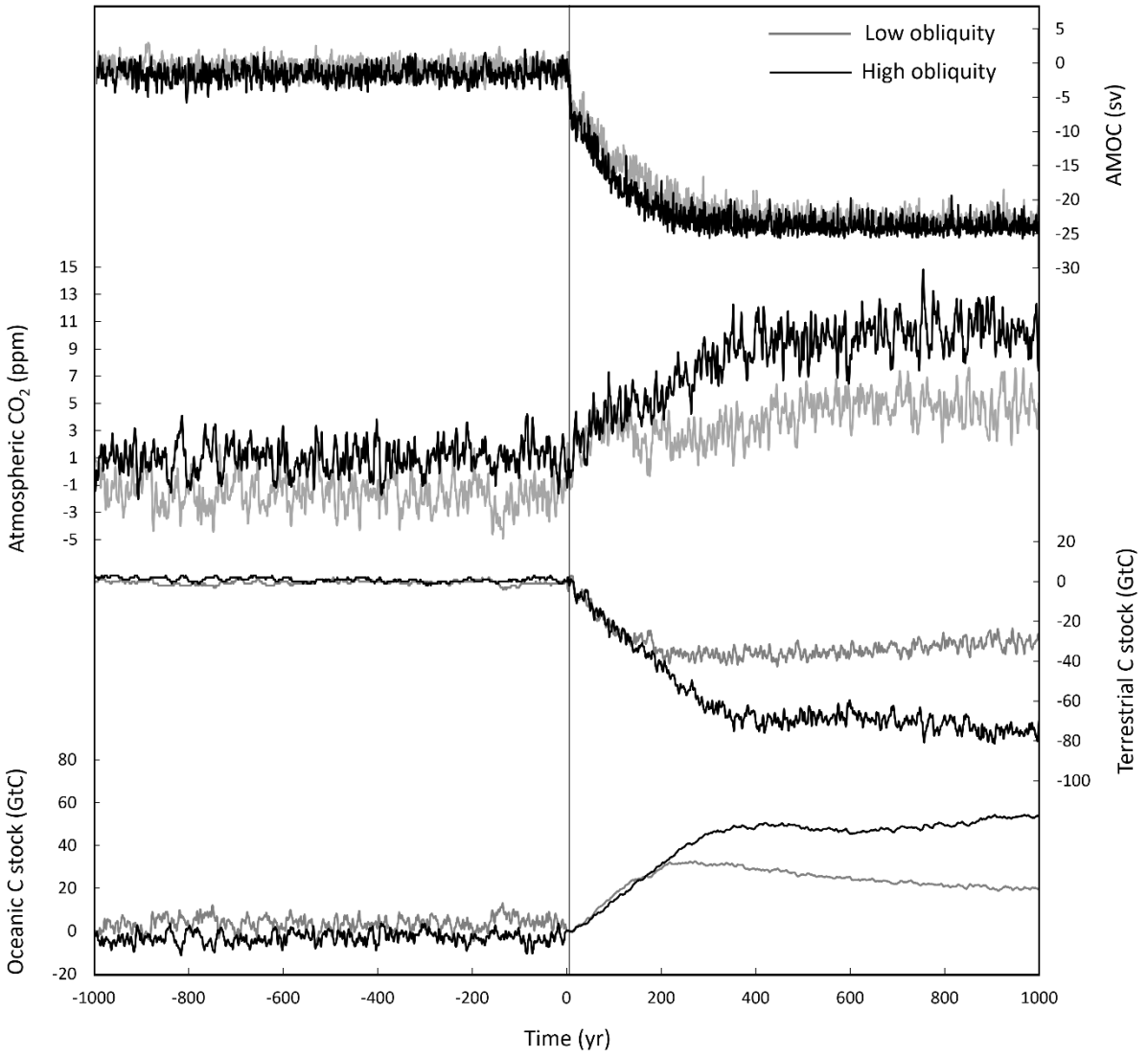


**Supplementary Figure 17:** Timeseries of (from top to bottom): AMOC transport (Sv), atmospheric $CO_2$ concentrations (ppm), oceanic carbon stock (GtC) and terrestrial carbon stock (GtC) for the high (black) and low (grey) obliquity control states. A negative time value corresponds to the model spin-ups, while a positive time value corresponds to the post-perturbation simulations. The y-axis is an anomaly respectively to the value for Time = 0.

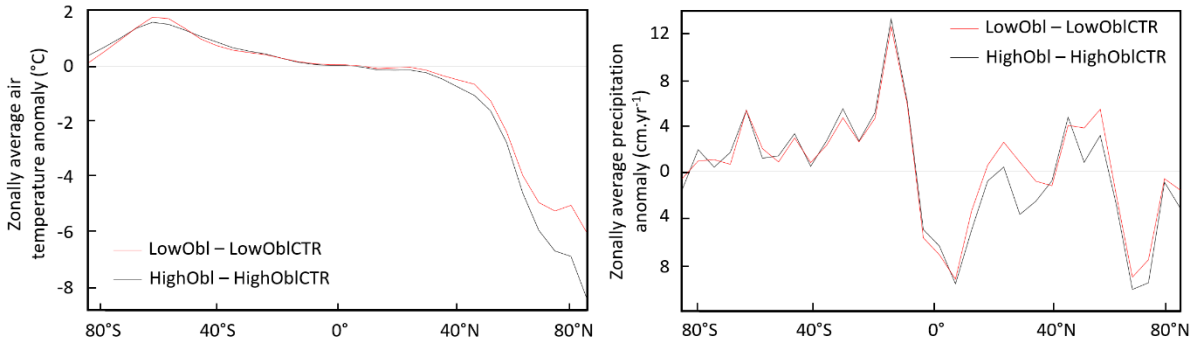


**Supplementary Figure 18:** Zonally averaged (left) air temperature anomaly (°C) and (right) precipitation anomaly (cm/yr) for (black) *HighObl* compared to *HighOblCTR* and (red) *LowObl* compared *LowOblCTR*. For *HighObl* and *LowObl*, the data has been averaged over simulation years 380 to 400.

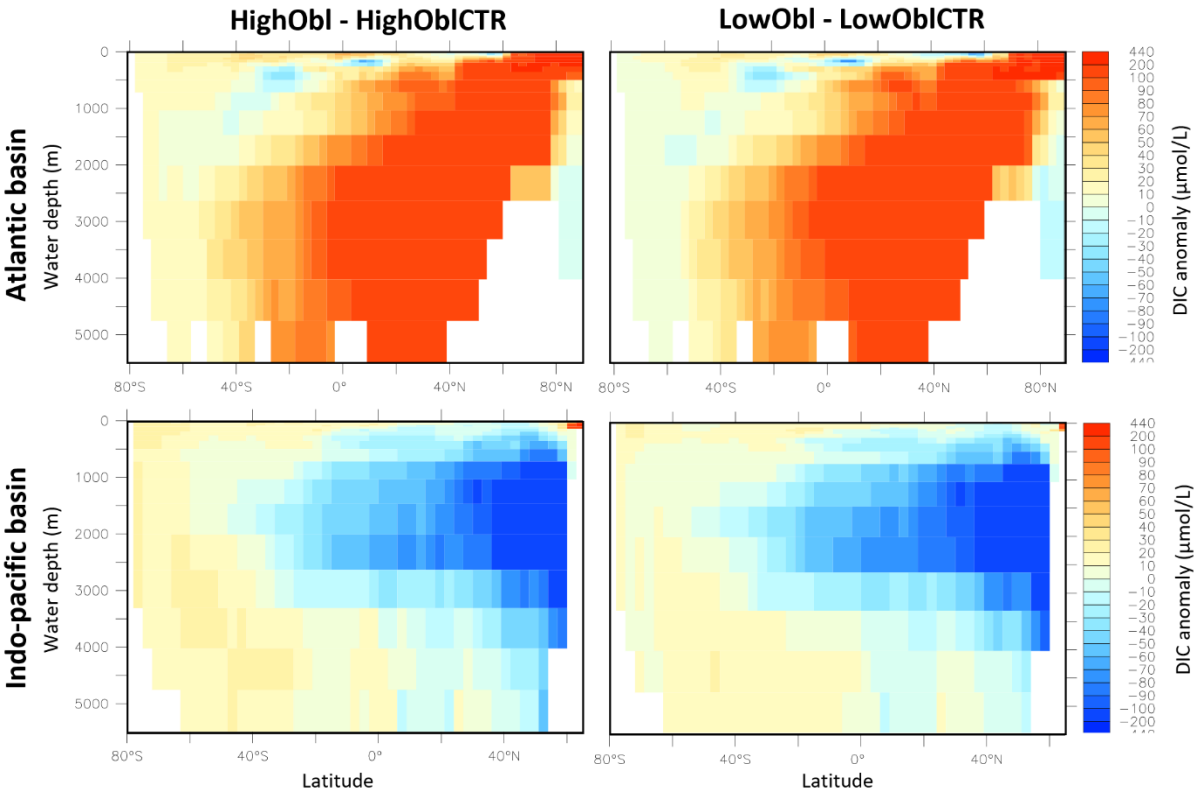


518

519 **Supplementary Figure 19:** DIC anomaly (µmol/L) averaged over (top) the Atlantic and (bottom) the Indo-Pacific
520 basin for (left) *HighObl* compared to *HighOblCTR* and (right) *LowObl* compared to *LowObl*.

521

522

523

524

525

526

527

528

529

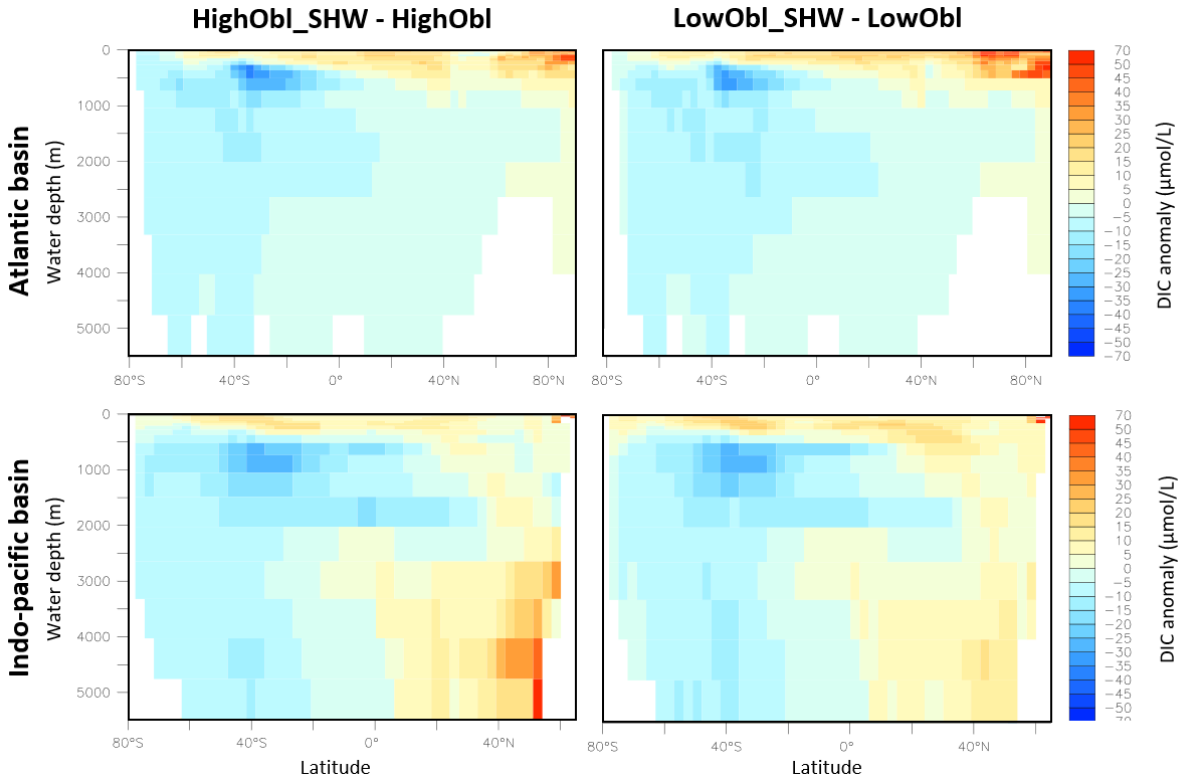


**Supplementary Figure 20:** DIC anomaly (µmol/L) averaged over (top) the Atlantic and (bottom) the Indo-Pacific basin for (left) *HighObl_SHW* compared to *HighObl* and (right) *LowObl_SHW* compared to *LowObl*.

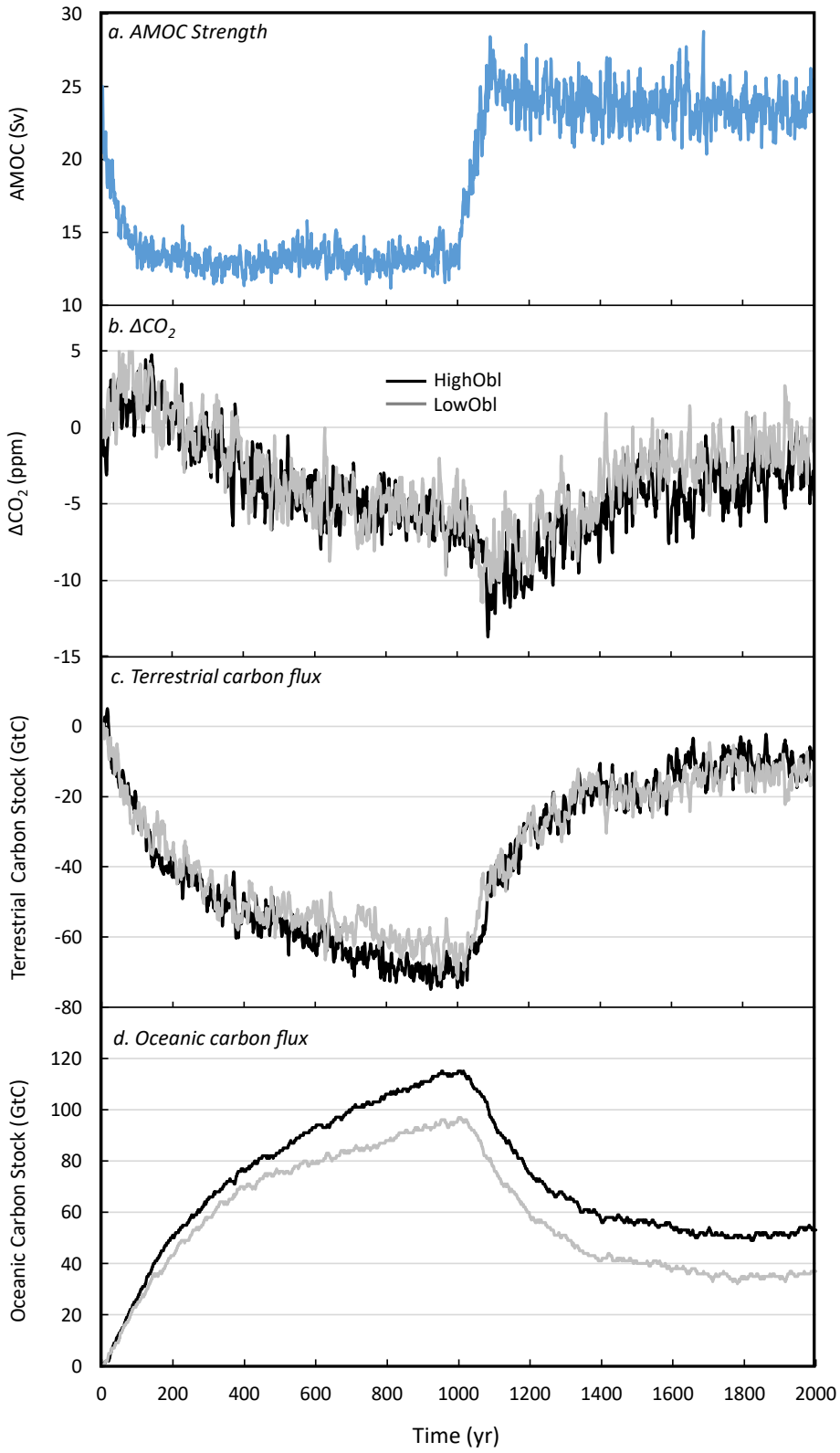


551

552 **Supplementary Figure 21: AMOC, $CO_2$ concentrations, and terrestrial and oceanic carbon changes in carbon**
553 **reservoirs during at 12 ka under high and low obliquity phase.** a. Atlantic Meridional Overturning Circulation
554 (AMOC) during the simulation. b. Atmospheric $CO_2$ concentrations during the simulation. *HighObl* (black) and
555 *LowObl* (grey) are performed under the obliquity at 12 ka (24.16°) and artificially low obliquity forcing (22.1°),
556 respectively. c. Terrestrial carbon stock (in GtC) from the start of the simulation until 2 ka. d. Similar to c. but for
557 oceanic carbon stock.

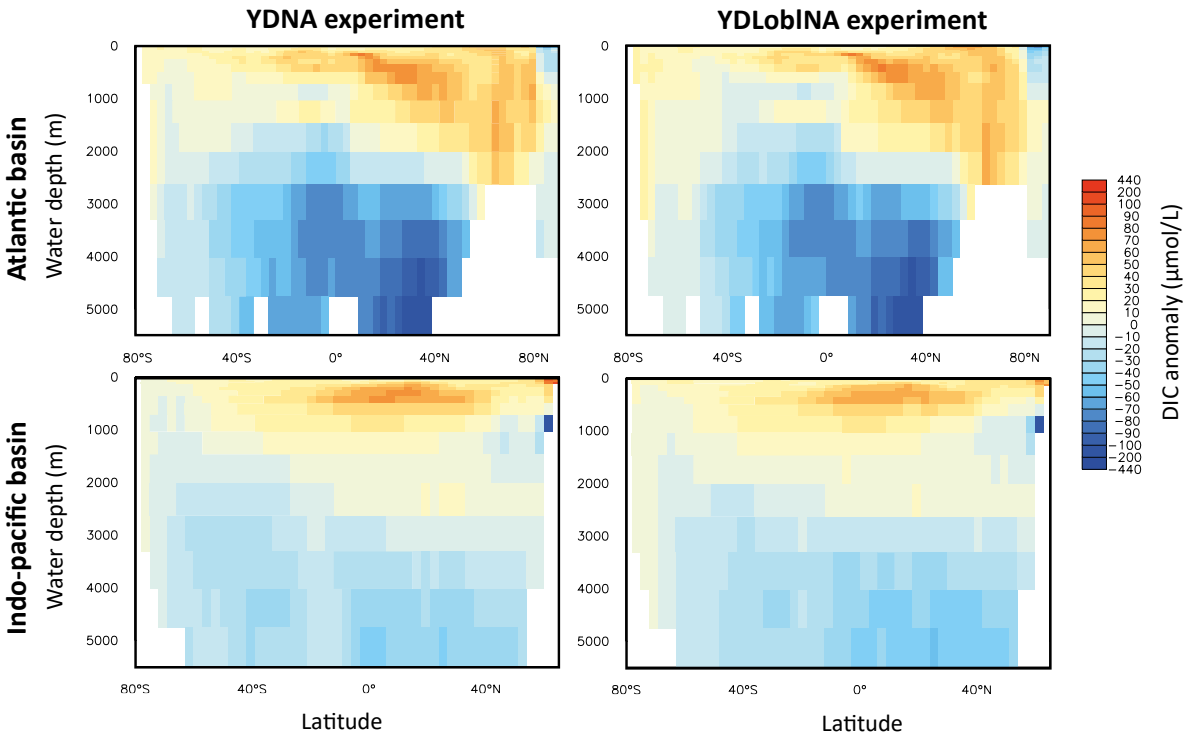


**Supplementary Figure 22:** DIC anomalies (µmol/L) as a result of the AMOC recovery (yr 1400-1600 when the AMOC has recovered compared to yr 800-1000 when the AMOC is off) averaged over (top) the Atlantic basin and (bottom) the Indo-Pacific for (left) experiment YDNA and (right) experiment YDLoblNA.

# Supplementary Tables

Supplementary Table 1: CDJs of the past 500 ka. Ages of CDJ are from the AICC2023 [13] chronology except for the six youngest CDJs that are on the WD2014 [36,37] and Taylor-adapted AICC2012 [30] chronology. Obliquity value is from ref. [17]. WDC: Wais Divide ice Core. EDC: EPICA Dome C ice core.

| CDJ name | CDJ age (ka) | Age uncertainty (ka, 1σ) | Obliquity (°) | Ice core | Reference |
|---|---|---|---|---|---|
| CDJ+ 2a.3 | 11.8 | 0.1 | 24.18 | WDC | Marcott et al. (2014) |
| CDJ+ 2a.2 | 14.7 | 0.2 | 23.92 | WDC | Marcott et al. (2014) |
| CDJ- 2a.1 | 16.3 | 0.2 | 23.72 | WDC | Marcott et al. (2014) |
| CDJ-3a.2 | 39.4 | 0.4 | 23.48 | WDC | Ahn et al. (2012) |
| CDJ-3a.1 | 48.4 | 0.4 | 24.44 | WDC | Bauska et al. (2021) |
| CDJ+5a | 72.1 | 2.5 | 22.40 | Taylor Glacier | Menking et al. (2022) |
| CDJ-6c | 160.6 | 1.0 | 23.52 | EDC | Shin et al. (2020) |
| CDJ+7a | 201.9 | 1.1 | 23.40 | EDC | *This study* |
| CDJ 7b | 205.0 | 1.1 | 23.87 | EDC | *This study* |
| CDJ 7c | 213.6 | 1.3 | 24.43 | EDC | *This study* |
| CDJ+7e | 243.0 | 0.7 | 23.55 | EDC | *This study* |
| CDJ-8.3 | 245.5 | 0.8 | 23.96 | EDC | *This study* |
| CDJ-8a.2 | 250.4 | 0.9 | 24.39 | EDC | *This study* |
| CDJ-8a.1 | 254.9 | 0.9 | 24.28 | EDC | *This study* |
| CDJ+9e | 334.3 | 0.8 | 24.22 | EDC | Nehrbass-Ahles et al. (2020) |
| CDJ-10a | 341.5 | 1.1 | 23.41 | EDC | Nehrbass-Ahles et al. (2020) |
| CDJ+11a.4 | 377.1 | 1.1 | 24.06 | EDC | Nehrbass-Ahles et al. (2020) |
| CDJ-11a.3 | 378.7 | 1.1 | 23.90 | EDC | Nehrbass-Ahles et al. (2020) |
| CDJ+11a.2 | 385.6 | 1.2 | 23.04 | EDC | Nehrbass-Ahles et al. (2020) |
| CDJ+11a.1 | 390.1 | 1.6 | 22.60 | EDC | Nehrbass-Ahles et al. (2020) |
| CDJ-11c | 417.0 | 1.9 | 24.25 | EDC | Nehrbass-Ahles et al. (2020) |
| CDJ+11e | 427.0 | 1.1 | 23.23 | EDC | Nehrbass-Ahles et al. (2020) |

Supplementary Table 2: Chi-square test at one degree of freedom and 10% of significance of the following hypothesis: *CDJ occurrences are independent from the average value of the last 500 ka of the tested parameter*. This hypothesis could be rejected at 90% of confidence only for obliquity.

| Tested parameter | $X^2$ test results |
|---|---|
| Obliquity | 3.4 > 2.7 |
| Precession | 0.5 < 2.7 |
| Eccentricity | 1.1 < 2.7 |
| Sea level | 0.1 < 2.7 |
| $CO_2$ | 0.1 < 2.7 |

Supplementary Table 3: Chi-square test at one degree of freedom of the null hypothesis that *CDJ occurrences are independent from the average value of the 12 obliquity cycles of the last 500 ka* when the CDJ events are displayed on three different gas age scales. The null hypothesis is rejected at the 90% confidence level (2.7) when the CDJ events are displayed onAICC2023 [13] and $\delta^{18}O_{calcite}$ chronology [16] and at the 95% confidence level (3.8) when displayed on AICC2012 [14].

| Considered chronology | $X^2$ test results |
|---|---|
| AICC2023 | 3.4 > 2.7 |
| AICC2012 | 4.6 > 3.8 |
| $\delta^{18}O_{calcite}$ | 3.4 > 2.7 |

Supplementary Table 4: Supplementary Table 4: Centennial-scale events with an amplitude larger than 3 ppm and a rate of change faster than 1.0 ppm/century over the past 500 ka. Bold lines are the CDJs discussed in this study, as defined in Ref. [9] with an amplitude larger than 5 ppm and a rate of change faster than 1.5 ppm.century$^{-1}$. Corresponding obliquity values associated with each of the centennial-scale events are indicated. 18 of those rapid events are associated with an obliquity value higher than 23.33° (i.e. the average obliquity value of the 12 obliquity cycles over the last 500 ka). Ages of CDJ are from the AICC2023 [13] chronology except for the 17 youngest CDJs that are on the WD2014 [36,37] and Taylor-adapted AICC2012 [30] chronology.

| Age (ka) | Obliquity (°) | Rate of change (ppm.century-1) | Amplitude (ppm) |
|---|---|---|---|
| **11.8** | **24.2** | **3.2** | **18.6** |
| 12.8 | 24.1 | 1.4 | 7.3 |
| **14.7** | **23.9** | **2.9** | **15.2** |
| **16.3** | **23.7** | **2.6** | **14.5** |
| 24.4 | 22.5 | 1.1 | 10.0 |
| 25.8 | 22.3 | 1.1 | 3.5 |
| 27.6 | 22.2 | 1.1 | 6.6 |
| 30.9 | 22.3 | 1.0 | 3.7 |
| 38.4 | 23.3 | 1.0 | 3.1 |
| **39.4** | **23.5** | **2.2** | **15.5** |
| 43.5 | 24.1 | 1.2 | 6.0 |
| 47.7 | 24.4 | 1.3 | 6.1 |
| **48.4** | **24.4** | **1.6** | **9.8** |
| 55.3 | 23.9 | 1.1 | 5.0 |
| 56.2 | 23.8 | 1.2 | 4.8 |
| 61.0 | 23.1 | 1.1 | 7.7 |
| **72.1** | **22.4** | **2.1** | **10.1** |
| 155.3 | 22.8 | 1.2 | 3.5 |
| **160.6** | **23.5** | **1.8** | **6.7** |
| 161.6 | 23.7 | 1.1 | 6.7 |
| 164.2 | 23.9 | 1.2 | 7.1 |
| 170.8 | 24.1 | 1.1 | 6.2 |
| 179.9 | 23.3 | 1.5 | 4.1 |
| 184.8 | 22.8 | 1.2 | 5.9 |
| **201.9** | **23.4** | **2.7** | **10.6** |
| **205.0** | **23.9** | **1.6** | **5.1** |
| **213.6** | **24.4** | **2.0** | **5.7** |
| 221.8 | 23.4 | 1.0 | 5.0 |
| 228.8 | 22.3 | 1.0 | 3.2 |
| 241.4 | 23.3 | 1.0 | 3.5 |
| **243.0** | **23.5** | **2.0** | **7.5** |
| 244.1 | 23.7 | 1.0 | 8.8 |
| **245.5** | **24.0** | **1.8** | **8.9** |
| 247.7 | 24.2 | 1.4 | 6.0 |
| **250.4** | **24.4** | **2.1** | **9.4** |
| 252.4 | 24.4 | 1.2 | 5.4 |
| **254.9** | **24.3** | **1.7** | **6.4** |
| **334.4** | **24.2** | **2.9** | **15.8** |
| **341.5** | **23.4** | **1.7** | **12.3** |
| 367.4 | 24.1 | 1.2 | 5.8 |
| **377.1** | **24.1** | **1.5** | **6.8** |
| **378.7** | **23.9** | **1.6** | **10.0** |
| **385.6** | **23.0** | **1.6** | **6.7** |
| **390.1** | **22.6** | **2.2** | **9.3** |
| **417.0** | **24.3** | **2.1** | **12.9** |
| **427.1** | **23.2** | **1.5** | **9.9** |
| 429.1 | 22.9 | 1.2 | 7.5 |

Supplementary Table 5: Description of the different LOVECLIM simulations and corresponding modelled $\Delta CO_2$ in ppm at year 400.

| *Simulation name* | *Details* | $\Delta CO_2$ (ppm) |
|---|---|---|
| *HighObl* | *49 ka Boundary conditions* | 9.5 |
| *LowObl* | *Similar to above under low obliquity phase* | 3.3 |
| *HighObl_NoVeg* | *No carbon flux between the terrestrial biosphere and atmosphere* | -0.1 |
| *LowObl_NoVeg* | *Similar to above under low obliquity phase* | 0.2 |
| *HighObl_SHW* | *Enhanced Southern Hemisphere westerly windstress (+40%)* | 14.2 |
| *LowObl_SHW* | *Similar to above under low obliquity phase* | 9.4 |
| *HighObl_NoVeg_SHW* | *No carbon flux between the terrestrial biosphere and atmosphere and enhanced Southern Hemisphere westerly windstress (+40%)* | 8.5 |
| *LowObl_NoVeg _SHW* | *Similar to above under low obliquity phase* | 9.8 |

# References


1. Petit, J. R. *et al.* Climate and atmospheric history of the past 420,000 years from the Vostok ice core, Antarctica. **399**, 10 (1999).
2. Bréant, C. *et al.* Unveiling the anatomy of Termination 3 using water and air isotopes in the Dome C ice core, East Antarctica. *Quaternary Science Reviews* **211**, 156–165 (2019).
3. Landais, A. *et al.* Interglacial Antarctic–Southern Ocean climate decoupling due to moisture source area shifts. *Nat. Geosci.* **14**, 918–923 (2021).
4. Landais, A. *et al.* Two-phase change in CO2, Antarctic temperature and global climate during Termination II. *Nature Geosci* **6**, 1062–1065 (2013).
5. Fischer, H., Wahlen, M., Smith, J., Mastroianni, D. & Deck, B. Ice Core Records of Atmospheric CO $_2$ Around the Last Three Glacial Terminations. *Science* **283**, 1712–1714 (1999).
6. Uemura, R. *et al.* Asynchrony between Antarctic temperature and CO2 associated with obliquity over the past 720,000 years. *Nat Commun* **9**, 961 (2018).
7. Ai, X. E. *et al.* Southern Ocean upwelling, Earth's obliquity, and glacial-interglacial atmospheric CO $_2$ change. *Science* **370**, 1348–1352 (2020).
8. Cheng, H. *et al.* Ice Age Terminations. *Science* **326**, 248–252 (2009).
9. Nehrbass-Ahles, C. *et al.* Abrupt $CO_2$ release to the atmosphere under glacial and early interglacial climate conditions. *Science* **369**, 1000–1005 (2020).
10. Marcott, S. A. *et al.* Centennial-scale changes in the global carbon cycle during the last deglaciation. *Nature* **514**, 616–619 (2014).
11. Bauska, T. K., Marcott, S. A. & Brook, E. J. Abrupt changes in the global carbon cycle during the last glacial period. *Nat. Geosci.* **14**, 91–96 (2021).
12. Rhodes, R. H. *et al.* Enhanced tropical methane production in response to iceberg discharge in the North Atlantic. *Science* **348**, 1016–1019 (2015).

13. Bouchet, M. *et al.* The Antarctic Ice Core Chronology 2023 (AICC2023) chronological framework and associated timescale for the European Project for Ice Coring in Antarctica (EPICA) Dome C ice core. *Clim. Past* **19**, 2257–2286 (2023).
14. Bazin, L. *et al.* An optimized multi-proxy, multi-site Antarctic ice and gas orbital chronology (AICC2012): 120–800 ka. *Clim. Past* **9**, 1715–1731 (2013).
15. Veres, D. *et al.* The Antarctic ice core chronology (AICC2012): an optimized multi-parameter and multi-site dating approach for the last 120 thousand years. *Clim. Past* **9**, 1733–1748 (2013).
16. Extier, T. *et al.* On the use of δ18Oatm for ice core dating. *Quaternary Science Reviews* **185**, 244–257 (2018).
17. Laskar, J. *et al.* A long-term numerical solution for the insolation quantities of the Earth. *A&A* **428**, 261–285 (2004).
18. Berger, A. & Loutre, M. F. Insolation values for the climate of the last 10 million years. *Quaternary Science Reviews* **10**, 297–317 (1991).
19. Menviel, L. C., Skinner, L. C., Tarasov, L. & Tzedakis, P. C. An ice–climate oscillatory framework for Dansgaard–Oeschger cycles. *Nat Rev Earth Environ* **1**, 677–693 (2020).
20. Okazaki, Y. *et al.* Deepwater Formation in the North Pacific During the Last Glacial Termination. *Science* **329**, 200–204 (2010).
21. Menviel, L. *et al.* Removing the North Pacific halocline: Effects on global climate, ocean circulation and the carbon cycle. *Deep Sea Research Part II: Topical Studies in Oceanography* **61–64**, 106–113 (2012).
22. Parrenin, F. *et al.* Synchronous Change of Atmospheric $CO_2$ and Antarctic Temperature During the Last Deglacial Warming. *Science* **339**, 1060–1063 (2013).
23. Menviel, L., England, M. H., Meissner, K. J., Mouchet, A. & Yu, J. Atlantic-Pacific seesaw and its role in outgassing $CO_2$ during Heinrich events: Heinrich $CO_2$. *Paleoceanography* **29**, 58–70 (2014).

24. Menviel, L. *et al.* Southern Hemisphere westerlies as a driver of the early deglacial atmospheric CO2 rise. *Nat Commun* **9**, 2503 (2018).
25. Loulergue, L. *et al.* Orbital and millennial-scale features of atmospheric CH4 over the past 800,000 years. *Nature* **453**, 383–386 (2008).
26. Spahni, R. *et al.* Atmospheric Methane and Nitrous Oxide of the Late Pleistocene from Antarctic Ice Cores. *Science* **310**, 1317–1321 (2005).
27. Enting, I. G. On the use of smoothing splines to filter $CO_2$ data. *J. Geophys. Res.* **92**, 10977 (1987).
28. Ahn, J., Brook, E. J., Schmittner, A. & Kreutz, K. Abrupt change in atmospheric $CO_2$ during the last ice age. *Geophys. Res. Lett.* **39**, (2012).
29. Shin, J. *et al.* Millennial-scale atmospheric CO<sub>2</sub> variations during the Marine Isotope Stage 6 period (190–135 ka). *Clim. Past* **16**, 2203–2219 (2020).
30. Menking, J. A. Multiple carbon cycle mechanisms associated with the glaciation of Marine Isotope Stage 4. *Nature Communications* (2022).
31. McManus, J. F., Oppo, D. W. & Cullen, J. L. A 0.5-Million-Year Record of Millennial-Scale Climate Variability in the North Atlantic. *Science* **283**, 971–975 (1999).
32. Bereiter, B. *et al.* Revision of the EPICA Dome C $CO_2$ record from 800 to 600 kyr before present: Analytical bias in the EDC CO2 record. *Geophys. Res. Lett.* **42**, 542–549 (2015).
33. Shin, J. *et al.* Millennial variations in atmospheric $CO_2$ during the early Holocene (11.7–7.4 ka). *Clim. Past* **18**, 2063–2075 (2022).
34. Bauska, T. K. *et al.* Links between atmospheric carbon dioxide, the land carbon reservoir and climate over the past millennium. *Nature Geosci* **8**, 383–387 (2015).
35. Berends, C. J., de Boer, B. & van de Wal, R. S. W. Reconstructing the evolution of ice sheets, sea level, and atmospheric CO<sub>2</sub> during the past 3.6 million years. *Clim. Past* **17**, 361–377 (2021).
36. Buizert, C. *et al.* The WAIS Divide deep ice core WD2014 chronology – Part 1: Methane synchronization (68–31 ka BP) and the gas age–ice age difference. *Clim. Past* **11**, 153–173 (2015).

37. Sigl, M. *et al.* The WAIS Divide deep ice core WD2014 chronology – Part 2: Annual-layer counting (0–31 ka BP). *Clim. Past* (2016).

38. Lüthi, D. *et al.* CO2 and O2/N2 variations in and just below the bubble–clathrate transformation zone of Antarctic ice cores. *Earth and Planetary Science Letters* **297**, 226–233 (2010).

39. Bereiter, B. *et al.* Mode change of millennial $CO_2$ variability during the last glacial cycle associated with a bipolar marine carbon seesaw. *Proc. Natl. Acad. Sci. U.S.A.* **109**, 9755–9760 (2012).